Defense Threat Reduction Agency
8725 John J. Kingman Road, MS
6201 Fort Belvoir, VA 22060-6201

DTRA-TR-23-19

TECHNICAL REPORT

Radiation Effects in Nanoscale Electromechanical Logic Devices and Pathways Toward Robust Computing in Extreme Conditions

Distribution Statement A. Approved for public release; distribution is unlimited.

November 2022

HDTRA1-19-1-0035

Prepared by: Philip Feng

University of Florida, Gainesville, FL 32611

REPORT DOCUMENTATION PAGE

1. REPORT DATE	2. REPORT TYPE	3. DATES COVERED START DATE	3. DATES COVERED END DATE
20220701	Final Report	20190814	20220219

4. TITLE AND SUBTITLE
Radiation Effects in Nanoscale Electromechanical Logic Devices and Pathways Toward Robust Computing in Extreme Conditions

5a. CONTRACT NUMBER	5b. GRANT NUMBER	5c. PROGRAM ELEMENT NUMBER
	HDTRA1-19-1-0035	
5d. PROJECT NUMBER	**5e. TASK NUMBER**	**5f. WORK UNIT NUMBER**

6. AUTHOR(S)
Feng, Philip

7. PERFORMING ORGANIZATION NAME(S) AND ADDRESS(ES)
University of Florida
Department of Electrical & Computer Engineering, Herbert Wertheim College of Engineering
P.O. Box 116200
Gainesville, FL 32611-6200, USA

8. PERFORMING ORGANIZATION REPORT NUMBER

9. SPONSORING/MONITORING AGENCY NAME(S) AND ADDRESS(ES)	10. SPONSOR/MONITOR'S ACRONYM(S)	11. SPONSOR/MONITOR'S REPORT NUMBER(S)
Defense Threat Reduction Agency 8725 John J Kingman Rd #6201 Forst Belvoir, VA 22060	DTRA	DTRA-TR-23-19

12. DISTRIBUTION/AVAILABILITY STATEMENT
Distribution Statement A. Approved for public release; distribution is unlimited

13. SUPPLEMENTARY NOTES

14. ABSTRACT

The main objective is to pursue fundamental knowledge, discovery, and understanding of how radiation impact nanoelectromechanical systems (NEMS) in silicon carbide (SiC) and other wide-bandgap (WBG) materials, and to identify and quantify the radiation effects on such NEMS devices (such as resonators and switches) and their characteristics in various dynamical operations.

15. SUBJECT TERMS
Radiation Effects, NEMS, SiC, wide-bandgap, nanostructures, resonant frequency, quality factor, Q-factor, built-in stress, Young's modulus, threshold voltage, leakage, defects, trapped charge, MEMS, GaN, logic devices, electromechanical, nanoscales

16. SECURITY CLASSIFICATION OF: a. REPORT	b. ABSTRACT	C. THIS PAGE	17. LIMITATION OF ABSTRACT	18. NUMBER OF PAGES
U	U	U	SAR	25

19a. NAME OF RESPONSIBLE PERSON	19b. PHONE NUMBER *(Include area code)*
Feng, Philip	(352) 294-6320

PREVIOUS EDITION IS OBSOLETE.

STANDARD FORM 298 (REV. 5/2020)
Prescribed by ANSI Std. Z39.18

INSTRUCTIONS FOR COMPLETING SF 298

1. REPORT DATE.
Full publication date, including day, month, if available. Must cite at least the year and be Year 2000 compliant, e.g. 30-06-1998; xx-06-1998; xx-xx-1998.

2. REPORT TYPE.
State the type of report, such as final, technical, interim, memorandum, master's thesis, progress, quarterly, research, special, group study, etc.

3. DATES COVERED.
Indicate the time during which the work was performed and the report was written.

4. TITLE.
Enter title and subtitle with volume number and part number, if applicable. On classified documents, enter the title classification in parentheses.

5a. CONTRACT NUMBER.
Enter all contract numbers as they appear in the report, e.g. F33615-86-C-5169.

5b. GRANT NUMBER.
Enter all grant numbers as they appear in the report, e.g. AFOSR-82-1234.

5c. PROGRAM ELEMENT NUMBER.
Enter all program element numbers as they appear in the report, e.g. 61101A.

5d. PROJECT NUMBER.
Enter all project numbers as they appear in the report, e.g. 1F665702D1257; ILIR.

5e. TASK NUMBER. Enter all task numbers as they appear in the report, e.g. 05; RF0330201; T4112.

5f. WORK UNIT NUMBER.
Enter all work unit numbers as they appear in the report, e.g. 001; AFAPL30480105.

6. AUTHOR(S). Enter name(s) of person(s) responsible for writing the report, performing the research, or credited with the content of the report. The form of entry is the last name, first name, middle initial, and additional qualifiers separated by commas, e.g. Smith, Richard, J, Jr.

7. PERFORMING ORGANIZATION NAME(S) AND ADDRESS(ES). Self-explanatory.

8. PERFORMING ORGANIZATION REPORT NUMBER. Enter all unique alphanumeric report numbers assigned by the performing organization, e.g. BRL-1234; AFWL-TR-85-4017-Vol-21-PT-2.

9. SPONSORING/MONITORING AGENCY NAME(S) AND ADDRESS(ES). Enter the name and address of the organization(s) financially responsible for and monitoring the work.

10. SPONSOR/MONITOR'S ACRONYM(S). Enter, if available, e.g. BRL, ARDEC, NADC.

11. SPONSOR/MONITOR'S REPORT NUMBER(S). Enter report number as assigned by the sponsoring/monitoring agency, if available, e.g. BRL-TR-829; -215.

12. DISTRIBUTION/AVAILABILITY STATEMENT. Use agency-mandated availability statements to indicate the public availability or distribution limitations of the report. If additional limitations/ restrictions or special markings are indicated, follow agency authorization procedures, e.g. RD/FRD, PROPIN, ITAR, etc. Include copyright information.

13. SUPPLEMENTARY NOTES. Enter information not included elsewhere such as: prepared in cooperation with; translation of; report supersedes; old edition number, etc.

14. ABSTRACT. A brief (approximately 200 words) factual summary of the most significant information.

15. SUBJECT TERMS. Key words or phrases identifying major concepts in the report.

16. SECURITY CLASSIFICATION. Enter security classification in accordance with security classification regulations, e.g. U, C, S, etc. If this form contains classified information, stamp classification level on the top and bottom of this page.

17. LIMITATION OF ABSTRACT. This block must be completed to assign a distribution limitation to the abstract. Enter UU (Unclassified Unlimited) or SAR (Same as Report). An entry in this block is necessary if the abstract is to be limited.

PREVIOUS EDITION IS OBSOLETE.

DTRA Basic Research Final Report
Please answer all sections of the document. You are welcome to use figures and tables to complement or enhance the text.
Period of Performance: August 14, 2019 – February 19, 2022.

Grant/Award #: HDTRA1-19-1-0035
PI Name: Philip Feng
Organization/Institution: University of Florida (UF), Vanderbilt University (Sub-Contract)
Project Title: Radiation Effects in Nanoscale Electromechanical Logic Devices and Pathways Toward Robust Computing in Extreme Conditions

What are the major goals of the project?
List the major goals of the project as stated in the approved application or as approved by the agency. If the application lists milestones/target dates for important activities or phases of the project, identify these dates and show actual completion dates or the percentage of completion. Generally, the goals will not change from one reporting period to the next. However, if the awarding agency approved changes to the goals during the reporting period, list the revised goals and objectives. Also explain any significant changes in approach or methods from the agency approved application or plan.

The overarching *objective* is to *pursue fundamental knowledge, discovery, and understanding of how radiation impact NEMS resonant and logic devices in SiC (in comparison with mainstream Si) and other wide-bandgap (WBG) materials, and to identify and quantify the radiation effects on such nanostructures and devices*, particularly on key properties such as resonant frequency, quality (*Q*) factor, built-in stress, Young's modulus, threshold voltage, leakage, defects, trapped charge, contact, and lifetime. The team's Option Years' effort is as follows.

Option Years' Central Theme and Approaches: *Theme: Radiation effects on SiC and WBG MEMS/NEMS resonators and switches*. The team is examining technologically important semiconductor materials (such as SiC and GaN, in comparison with mainstream Si) in which the grantee has built extensive experience, available structures and testing data, available sets of lithographic design patterns, and proven fabrication protocols to obtain additional copies of the testing structures for probing radiation effects. The materials comparison (SiC *vs* Si with same designs) is particularly useful to delineate material specific mechanisms and identify strengths and weaknesses. As such, we are looking at different test structures which translate into NEMS resonators, resonant switches, logic switches, logic gates, and non-volatile (NV) storage elements. We will examine how radiation might *enhance* or *retard* the processes that lead to the common wear-out mechanisms in NEMS resonant and logic devices. The grantee will apply selected radiation and reliability tests, based on what might be particular strengths and weaknesses given the constituent crystals and the devices' modes of operation, to characterize the impacts of radiation. The grantee will leverage devices and design already proven and in hands (from previous DARPA program and earlier phases of this project), but will also fabricate additional structures, especially new co-fabricated SiC and Si NEMS.

What was accomplished under these goals?
For this reporting period describe: 1) major activities; 2) specific objectives; 3) significant results, including major findings, developments, or conclusions (both positive and negative); and 4) key outcomes or other achievements. Include a discussion of stated goals not met. As the project progresses, the emphasis in reporting in this section should shift from reporting activities to reporting accomplishments.

1. Overview and Brief Summary of the Accomplishments

(1) **Major Activities**:

Effort on SiC NEMS (see Annual Report of 2020) and Other Wide-Bandgap NEMS Devices

a. Design and fabrication of GaN/AlN heterostructure NEMS resonators.
b. Study of frequency response of GaN/AlN NEMS resonators to temperature variations.
c. Investigation of Ar^+ radiation effects in GaN doubly-clamped string resonators.
d. Design and fabrication of β-Ga_2O_3 vibrating channel transistors.
e. Study of ultraviolet light radiation effects on β-Ga_2O_3 transistor and NEMS resonator.
f. *In-Situ* electrical measurement of proton radiation effects on Si MEMS resonators.
g. Proton radiation effects on optically transduced SiC microdisk resonators.

(2) **Specific Objectives**:

a. Investigations of moderate energy radiation on MEMS and NEMS devices made by wide bandgap (WBG) and ultrawide bandgap (UWBG) materials. Particles with moderate energy level, *e.g.*, ultraviolet photons and heavy ions with energy < 1 MeV, are used to introduce radiation that can be absorbed by or interact with the device structure. Such investigation can provide information on how MEMS and NEMS device react when radiation interact strongly with the device structure, deepen the understanding in failure mechanisms and possible radiation sensing scenarios for WBG and UWBG MEMS and NEMS devices.

b. Explore and develop *in-situ* electrical measurement techniques for timely measure and monitor the responses of MEMS/NEMS devices under exposure to heavy ions radiation (*e.g.*, Pelletron from radiation system at Vanderbilt University).

(3) **Significant Results**:

a. Radiation Effects in GaN/AlN Doubly-Clamped String Resonators
We demonstrate the effects of 440 keV argon ion (Ar^+) on GaN/AlN doubly-clamped string resonators. We measure the resonance frequencies of the unirradiated and irradiated devices through optical interferometry. By comparing the resonance frequencies, the irradiated devices show significant downshifts in resonance frequency with respect to that of the unirradiated devices. Preliminary analysis suggests that the frequency downshifts are resulted from radiation induced stress and Young's modulus changes and deformation of suspended structure.

b. Radiation Effects in β-Ga_2O_3 Nanoelectromechanical Resonators
We design, fabricate and measure the beta gallium oxide (β-Ga_2O_3) NEMS resonators. We study the solar-blind ultraviolet light radiation effects *in situ* on such devices, including real-time monitoring of photocurrent and resonance frequency. In addition, we experimentally extract the Young's modulus of β-Ga_2O_3 as a baseline for future study on radiation effects on mechanical properties of β-Ga_2O_3 NEMS resonators. Finally, we construct the equivalent circuit model of β-Ga_2O_3 vibrating channel transistor as a platform in preparation for *in situ* measurement of radiation effects on β-Ga_2O_3 NEMS devices.

c. *In-Situ* Electrical Measurement of Proton Radiation Effects on Si MEMS Resonators
We have demonstrated *in-situ* measurement and monitoring of proton radiation effects on single-crystal silicon comb-drive resonant microelectromechanical systems (MEMS). The comb-drive resonators are specially designed and can be operated in both linear and contact-impacting (i.e., 'tapping') modes, which offer versatile options for resonant sensing and switching applications. In-situ, continuous monitoring of radiation effects induced by impinging 1.8MeV protons with controlled dosage and exposure time, in both linear and tapping modes of the resonators, have been performed. The resonators exhibit highly sensitive responses in resonance characteristics while maintaining robust operations.

2. Description of the Major Activities and Accomplishments

(1) Radiation Effects in **GaN Doubly-Clamped String Resonators**

We report on the investigation of the resonance behaviors and effects of stopped ion in gallium nitride (GaN) doubly-clamped string resonators. The investigation implies that the stopped ions have minimal effect on mass of the resonator while significantly alters the built-in stress and Young's modulus in the device, inducing pronounced resonance frequency downshifts.

a. Device Fabrication

We use GaN/AlN wafers (purchased from Kyma Technologies, Inc.) that consist of a crystalline GaN layer (500 nm) grown by hydride vapor phase epitaxy (HVPE) on top of an intermediate nucleation layer of AlN (200 nm) on standard Si (111) substrate. As illustrated in Fig. I-1, the fabrication of GaN/AlN strings starts from the deposition of chromium (Cr), followed by photolithography to define the Cr hard mask. We perform dry anisotropic etching with the Cr mask, through GaN and AlN layers, to define the doubly-clamped structures, followed by wet etching of Cr. After removal of Cr, we deposit and pattern the titanium (Ti) and aluminum (Al) electrode pads. Finally, we release the GaN/AlN heterostructure devices by isotropic dry etching of Si in xenon difluoride (XeF_2). Fig. I-1g displays an SEM image of as-fabricated devices, with thickness $t = 700$ nm, width $w = 5$ μm, and lengths $L = 100$, 200, and 300 μm.

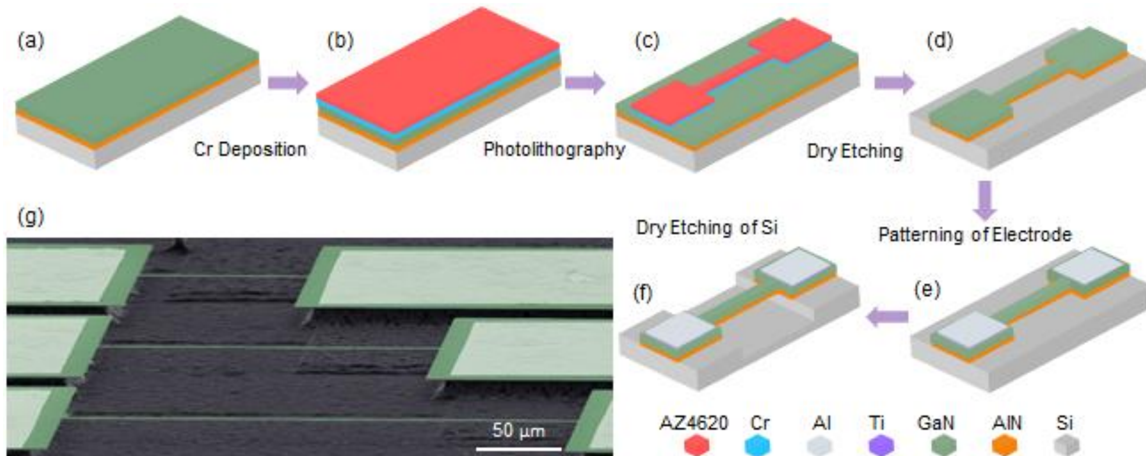

Figure I-1. (a)-(f) Microfabrication of the doubly-clamped GaN/AlN structures via a two-step lithographic process followed by device release in XeF_2 dry etching. (g) An SEM image of suspended GaN/AlN heterostructure micro strings with various lengths.

b. Temperature Coefficient of Resonance Frequency

We report on the first experimental characterization and analysis of the thermal response and temperature coefficient of resonance frequency (TC*f*) of gallium nitride/aluminum nitride (GaN/AlN) heterostructure micro string resonators, in a wide temperature range from -10 ºC up to 325 ºC. We design and fabricate GaN/AlN heterostructure micro string resonators with length *L* = 100, 200 and 300 μm to probe the stress and thermal effects on resonance behavior. All out-of-plane flexural modes show clear string behavior, and the multimode resonance frequencies downshift almost linearly with increasing temperature up to 325 ºC. The linear temperature dependence and TC*f* values of GaN/AlN heterostructure resonators can be directly employed for thermal sensing.

The multimode resonances of the GaN/AlN devices are measured by using a laser interferometry system, as shown in Fig. I-2a. An intensity-modulated 405 nm blue diode laser is utilized to photothermally drive the device motion, and a 633 nm He-Ne laser is employed to detect the vibration. Dynamic interference happens between the light reflected by the vibrating string and that by the substrate surface below the suspended structure. Thus, the motion of the device is transduced by the interferometric effect into intensity variation of the reflected 633 nm light. The photodetector converts the optical signal into electrical signal, which is monitored by a network analyzer. We regulate the temperature of the GaN/AlN device by using a Peltier thermoelectric heater/cooler; and the temperature of the chip is measured by a Si diode temperature sensor (Lake Shore DT-670). All the measurements are performed in a moderate vacuum of ~80 mTorr. To study the effects of resonance modes on TC*f*, we first characterize the multimode resonance of a 100μm-long device, including both out-of-plane and in-plane modes. Figure I-2b shows the multimode resonances of the 100μm-long device measured at room temperature. Five resonance modes are observed in the range of 1.5 to 7 MHz. By matching the resonance frequencies to finite element method (FEM) simulation results, the first two modes are out-of-plane flexural modes while the third one is an in-plane flexural mode. Between the measured fourth and fifth modes, one of them is the third out-of-plane flexural mode.

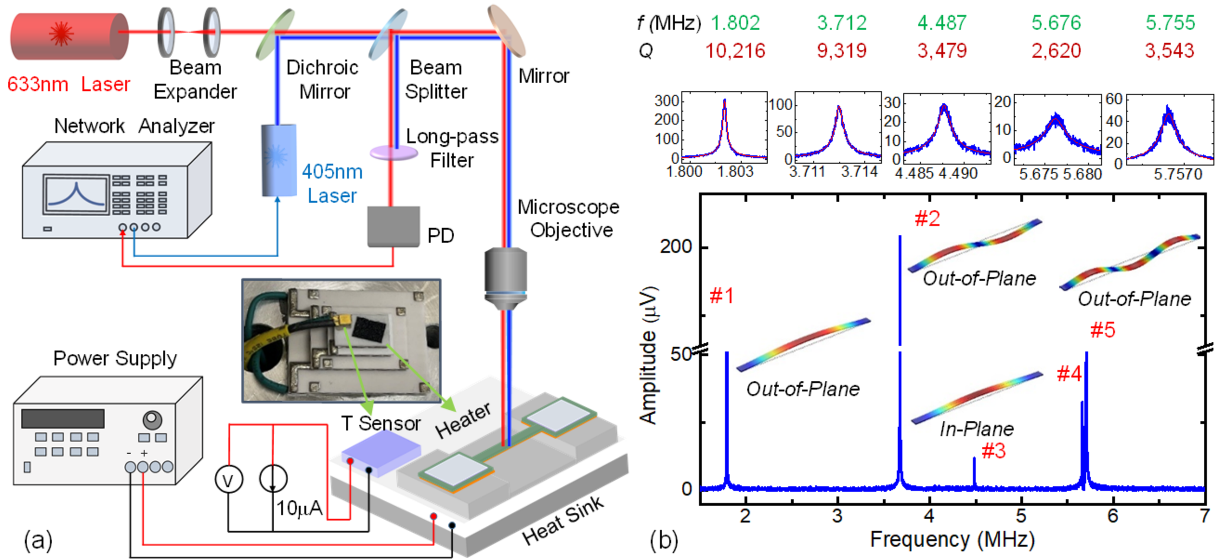

Figure I-2. Illustration of the ultrasensitive laser interferometry measurement system configured with a precisely temperature-controlled device stage. (b) Measured resonance spectra of a 100μm-long GaN/AlN string at room temperature, with panels above showing the zoom-in spectra of 5 modes with fitting curves. Insets show the corresponding simulated mode shapes.

We first characterize the TC*f* of the out-of-plane modes. Figure I-3 shows the resonance spectra of the first two modes measured in temperature range of -10 to 105 ºC. We find that the resonance frequencies increase gradually with decreasing temperatures. By plotting the

frequency shift at different temperatures with respect to its resonance frequency at 25.6 °C for each mode (Fig. I-3d & I-3g), we observe linear relation between $\Delta f/f$ and T among most of the measured temperatures. In this range, we extract an average TCf_1 of -336 ppm/ºC for the fundamental mode and TCf_2 of -316 ppm/ºC for the second mode. No clear trend of Q change is observed (Fig. 6b). According to the frequency ratio of the first two modes ($f_2/f_1 \approx 2$), the out-of-plane modes can be precisely described by using the string model (with $\sigma \approx$700 MPa).

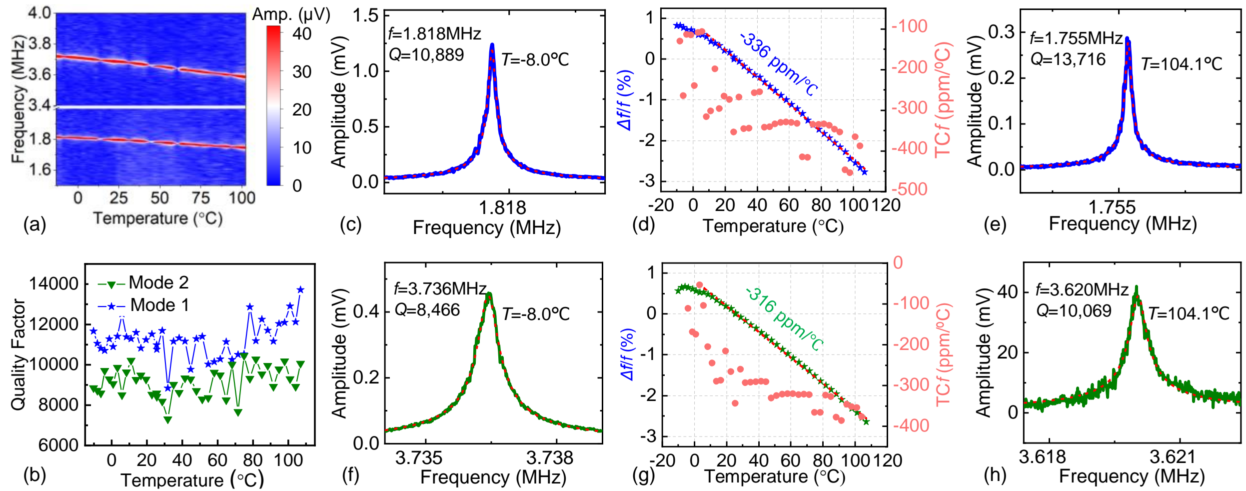

Figure I-3. The first two out-of-plane resonance modes and TCf measured from a device with length L = 100 µm. (a) Color plot of the resonance spectra for the first two modes measured with varying temperature. (b) Measured Q versus temperature. Measured (c) first mode and (f) second mode resonances at -8.0 °C. (d) and (g) Fractional frequency shift with varying temperature. Measured (e) first mode and (h) second mode resonance at 104.1 °C.

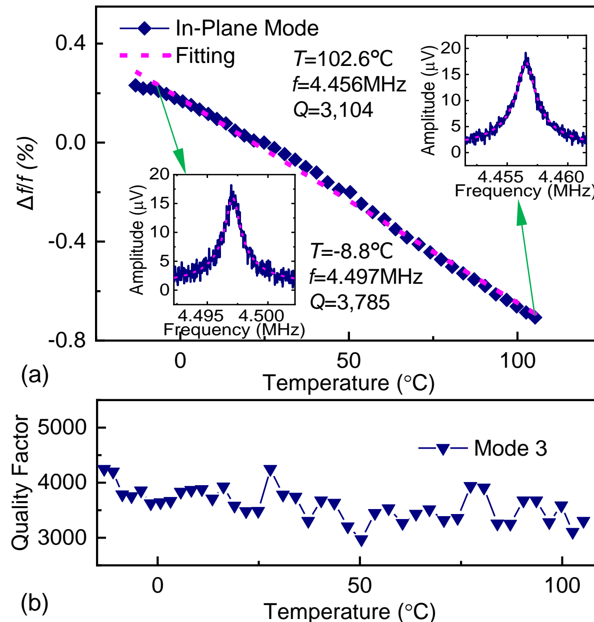

Figure I-4. Measured in-plane flexural mode resonance and TCf. (a) Fractional frequency shift versus temperature from -10 to 105°C. *Insets* show resonance spectra at selected temperatures. (b) Measured Q versus temperature.

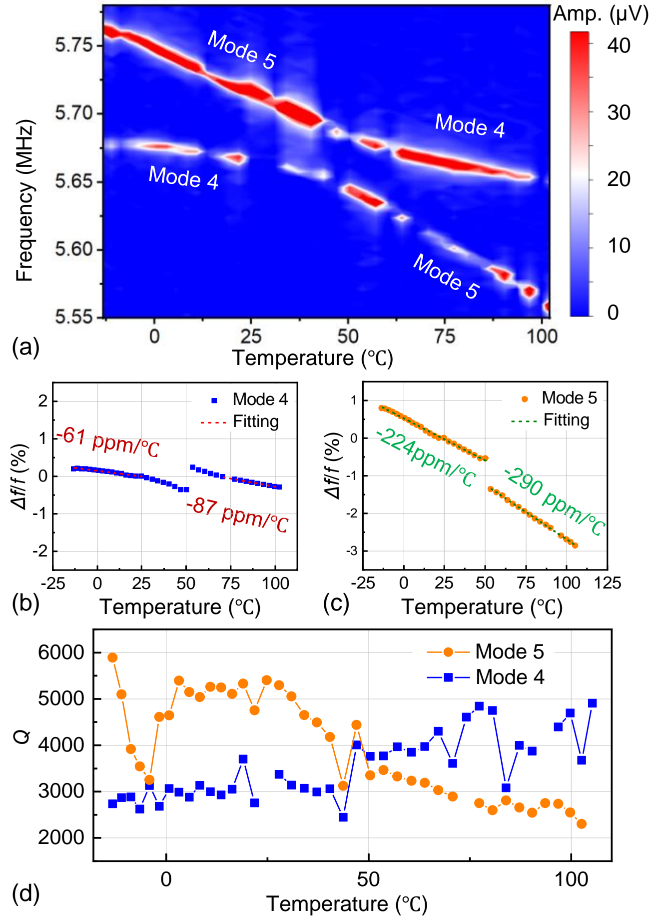

Figure I-5. Measured resonance characteristics of the 4th and 5th flexural modes and TC*f*. (a) Resonance spectra at different temperatures from -10 to 105°C. Fractional frequency shift versus temperature for (b) the 4th mode and (c) the 5th mode. (d) Measured *Q* versus temperature, for both the 4th and 5th modes.

To further investigate frequency response of the GaN/AlN doubly-clamped structure, we also measure the temperature dependence of the first in-plane (lateral) flexural mode (3rd mode overall, f_3). We observe much smaller frequency shift as temperature varies (than in the earlier two modes). As shown in Fig. I-4a, f responds linearly to sweeping T in the measured T range with an averaged TCf_3 = -83 ppm/^{o}C, less than 1/3 of earlier measured values for out-of-plane modes (TCf_1 and TCf_2). Based on the cross-sectional shape (rectangular) and orientation of the doubly-clamped structure, the flexural rigidity in the in-plane direction ($E_Y I_z = E_Y t w^3/12$) is more than fifty time larger than that in the out-of-plane direction ($E_Y I_y = E_Y w t^3/12$). Thus, the in-plane mode resonance frequency, f_3, depends more on E_Y of the material than on the built-in stress σ, compared to the two out-of-plane flexural modes (f_1 and f_2). The shift of resonance frequency caused by the change of built-in stress (induced by thermal expansion) can be partly compromised by the frequency modulation induced by Young's modulus change (governed by TCE_Y), leading to a smaller TCf for the in-plane mode. The Q of the in-plane mode is also generally stable, with minor declination, over the varying temperature range (Fig. I-4b).

Figure I-5 shows the frequencies of both the 4th and 5th modes as functions of temperature, in which we observe clear anti-crossing between the modes. The anti-crossing point appears at ~50 ^{o}C. The average TCf for the 4th mode is about -74 ppm/^{o}C and the average TCf for the 5th mode is about -250 ppm/^{o}C. According to the TCf values, we infer the anti-crossing occurs between an in-plane mode (4th mode) and an out-of-plane mode (5th mode). In contrast to the Q curves of the

first three modes, the measured Q of the 4th mode increases, while the Q of the 5th mode declines in the temperature range of -10 to 105 ºC (see Fig. I-5d).

In summary, we have designed GaN/AlN heterostructure micro string resonators with lengths L = 100, 200 and 300 μm to probe the stress and thermal effects on resonance behavior. The resonances of out-of-plane modes show clear string behavior. By tracking the temperature dependence of multimode resonances, we have found the frequencies downshift almost linearly with increasing temperature up to 325 ºC. For a given device, the out-of-plane modes show similar TCf values, which are three times larger than that of the in-plane mode. The longer devices tend to have larger TCf values. We observe the largest TCf value of about -500 ppm/ºC in a 300μm-long device. The linear temperature dependence and TCf values of GaN/AlN heterostructure resonators can be directly employed for thermal sensing.

c. Ion-Induced Displacement Damage on GaN/AlN MEMS Resonators

We report on the effects of ion radiation-induced displacement damage on GaN/AlN doubly-clamped resonant MEMS. We design and fabricate GaN/AlN heterostructure MEMS resonators with lengths L = 100, 200, 300, 400, 500, 600, and 700 μm, and irradiate the devices by 440 keV Ar^+ ions with fluences of 5×10^{11}, 5×10^{12}, 10^{13}, 10^{14}, and 10^{15} cm^{-2}, to probe the effects of ion radiation-induced displacement damage on resonance behavior. Stopping and Range of Ions in Matter (SRIM) simulation shows that displacement damage is confined in the GaN layer. The multimode resonances of the devices decrease significantly (>50%) with the increase of fluence beyond 10^{14} cm^{-2}. According to SEM images, the highly irradiated (fluence above 10^{14} cm^{-2}) GaN/AlN resonators are severely curved, where the amount of curvature increases monotonically with the increase of fluence. The results extend the understanding of radiation-induced damage mechanisms in GaN MEMS devices.

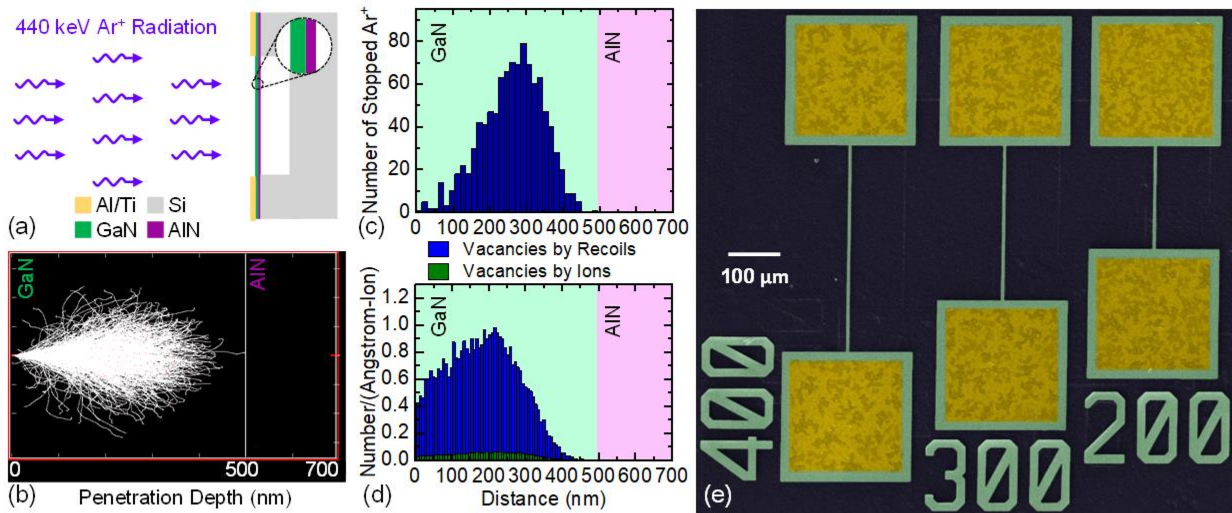

Figure I-6. (a) 440 keV Ar^+ radiation on GaN/AlN devices. (b) SRIM simulation of 1,000 Ar^+ ions on GaN/AlN structure. (c) Distribution of stopped Ar^+ ions. (d) Distribution of displacement damage induced vacancies. (e) An SEM image of suspended GaN/AlN doubly-clamped resonators with various lengths.

We design a set of experiments to systematically study the displacement damage on GaN/AlN MEMS resonators. First, argon ions (Ar^+) with energy of 440 keV are chosen as irradiation source to introduce displacement damage within GaN layer. Then the crystallinity and stress change in GaN thin film under the effect of radiation are tracked via Raman spectroscopy. Doubly-clamped GaN/AlN MEMS resonators with different length are used to investigate the radiation effect on mechanical properties. By tracking the resonance frequency of GaN/AlN resonators, the built-in stress and Young's modulus can be extracted, which are good representation of mechanical

properties of the devices. Finally, scanning electron microscope (SEM) is utilized to characterize the morphology of the GaN/AlN resonators before and after the ion irradiation.

To assure that major displacement damage events occur in the GaN/AlN device layer, the energy and ion species are selected so that the ions stop within the GaN/AlN heterostructure (Fig. I-6a). Argon ions (Ar^+) with energy of 440 keV are chosen to irradiate the MEMS devices. Simulation by the stopping and range of ions in matter (SRIM) code shows that all the 440 keV Ar+ ions stop in the GaN layer (Fig. I-6b & I-6c) and the displacement damage (creation of vacancies) is confined in the GaN thin film (Fig. I-6d). We irradiate GaN/AlN MEMS devices with fluences of 5×10^{11}, 5×10^{12}, 10^{13}, 10^{14} and10^{15} cm^{-2} 440 keV Ar+.

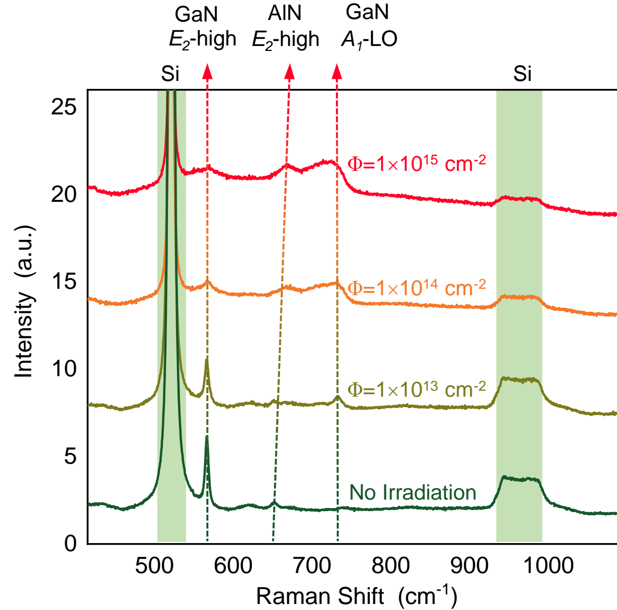

Figure I-7. Raman spectra of GaN/AlN heterostructure on Si (111) substrate with and without irradiation.

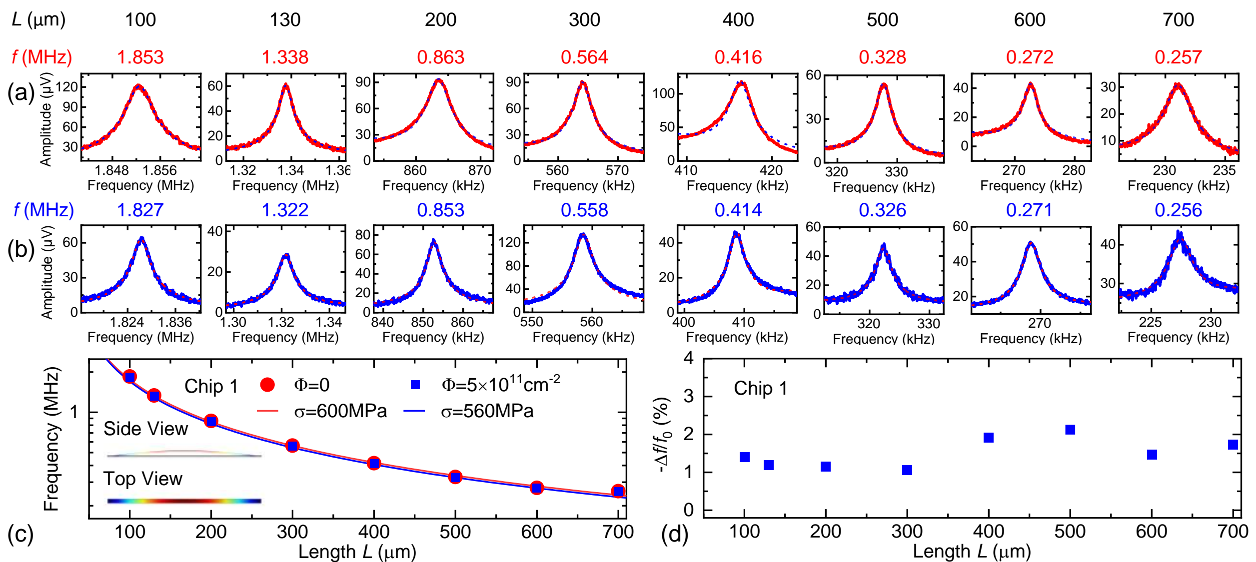

Figure I-8. Fundamental mode resonance spectra of devices with L = 100, 130, 200, 300, 400, 500, 600, and 700 μm (a) before and (b) after radiation with fluence of 5×10^{11} cm^{-2}. (c) Resonance frequency fitting with elastic resonator model (Eq. 1). (d) Fractional downshift of resonance frequency.

To understand the effect of radiation on the crystallinity of GaN and built-in stress in GaN layer, Figure I-7 shows the Raman spectra of the GaN/AlN heterostructure on Si (111) substrate for both unirradiated and irradiated samples with fluences of 10^{13}, 10^{14} or 10^{15} cm^{-2}. Consistent with literature reports, both the E_2-high and A_1–LO modes of GaN are observed at 566.4 and 733.3 cm^{-1}, respectively for unirradiated sample. The shift of E_2-high phonon mode can be utilized to quantify the stress in GaN. For stress free GaN film, the E_2-high mode should be at 567.6 cm^{-1}. The blue shift of E_2-high mode postulates that stress in the GaN layer is tensile in nature. The E_2-high mode peak of GaN gradually broadens with the increase of the fluences of radiation, implying reduced crystallinity. It suggests that at high fluence (≥ 10^{14} cm^{-2}) of radiation, crystalline GaN become amorphous. Moreover, we assign the peak at 651.3 cm^{-1} to be the E_2-high mode of the AlN. The Raman peak positions are fluence dependent, implying stress alteration by radiation.

The flexural resonance frequency of the fundamental mode of the GaN/AlN doubly-clamped resonator can be expressed as

$$f_0 = \frac{9\pi}{8L^2}\sqrt{\frac{E_Y I}{\rho w t}}\sqrt{1+\frac{0.24\sigma w t L^2}{\pi^2 E_Y I}} , \tag{1}$$

where $I = wt^3/12$ is the moment of inertia, L, w, and t are length, width, and thickness of the doubly-clamped device, respectively, E_Y and ρ are the averaged Young's modulus and the averaged mass density of the GaN/AlN heterostructure, respectively, and σ is the built-in stress in the suspended structure. We first measure and model the fundamental mode resonance of unirradiated GaN/AlN doubly-clamped resonators, with L=100 μm, 130 μm, 200 μm, 300 μm, 400 μm, 500 μm, 600 μm, and 700 μm. The fundamental mode resonance frequencies are centered at 1.853 MHz, 1.338 MHz, 0.863 MHz, 0.564 MHz, 0.416 MHz, 0.328 MHz, 0.272 MHz, and 0.257 MHz, respectively (Fig. I-8a). The measured resonance frequencies agree well with the analytical model (Eq. 1) by using $E_{Y,GaN}$ = 360 GPa, $E_{Y,AlN}$ = 344 GPa, ρ_{GaN} = 6150 kg/m^3, ρ_{AlN} = 3260 kg/m^3, and σ = 600 MPa. We then radiate the devices with fluence of 5×10^{11} cm^{-2} and measure the fundamental mode resonance frequencies. The resonance spectra and fractional downshift of resonance frequency shown in Fig. I-8. The fractional downshift of resonance frequencies of fundamental mode lies within the range of 1% and 2.5%. According to the theoretical analysis, it is reasonable to suggest that the deteriorated resonance properties should be related to the variation of built-in stress and Young's modulus under radiation conditions.

To further study the radiation effect on the resonance of fundamental mode, we increase the fluence to 10^{13} cm^{-2}, 10^{14} cm^{-2}, and 10^{15} cm^{-2}. Figure I-9 show the fundamental mode resonance spectra of 300 μm and 400 μm long devices before and after radiation with the fluences of 10^{14} cm^{-2}. Taking 300 μm long device as an example, the fundamental mode resonance frequency decreases from 499 to 124 kHz after radiation. Similar trends are observed from the devices with different lengths. Compared with the results shown in Fig. I-8, the frequency downshifts much more dramatically for the devices irradiated with higher fluences, specifically, ~20% downshift for fluence of 10^{13} cm^{-2}, ~70% downshift for fluence of 10^{14} cm^{-2}, ~80% downshift for fluence of 10^{15} cm^{-2}. An earlier study suggests that the GaN crystal can become amorphous after high fluence ion radiation. Therefore, if we use the same analytical model and apply the Young's modulus of amorphous GaN, $E_{Y,GaN}$ = 65 GPa, into Eq. (1), we obtain the fundamental mode resonance frequency scaling as a function of built-in stress (Fig. I-9e). By using the experimentally measured resonances into the analytical model, we extract the built-in stress of the devices after radiation. For fluences ≥ 10^{14} cm^{-2}, the post-radiation built-in stress decreases significantly from 440 MPa to ~10–70 MPa. For a fluence of 10^{13} cm^{-2}, a comparably moderate built-in stress change from 440 MPa to ~330 MPa is induced in the 200 μm long devices. The results suggest that at high fluences (⩾ 10^{14} cm^{-2}), the mechanical properties of GaN/AlN MEMS resonators can be severely altered by displacement damage. Figure I-10 summarizes the effect of radiation fluence on

fractional downshift of resonance frequency. For fluence is equal or less than 10^{13} cm^{-2}, fractional downshift of resonance frequency is exponentially related to dosage level. For fluence is equal or larger than10^{14} cm^{-2}, frequency shift saturates. As will discussed later, this can be ascribed to the strong deformation of GaN/AlN devices at extremely high irradiation (fluence ≥ 10^{14} cm^{-2}).

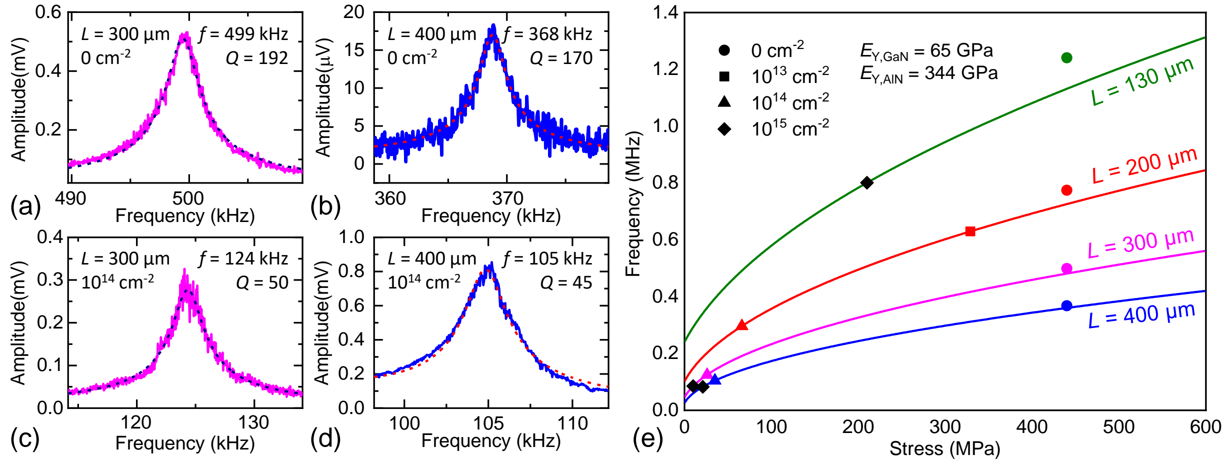

Figure I-9. (a) & (b) Fundamental mode resonance spectra of unirradiated 300 and 400 μm long devices, respectively. (c) & (d) Fundamental mode resonance spectra of the devices after 10^{14} cm^{-2} of 440 keV Ar^+ radiation. (e) Comparison of measured and calculated fundamental mode resonance frequencies at varying stress with $E_{Y,GaN}$ = 65 GPa. Symbols represent the measured frequencies while the lines represent the calculated frequencies.

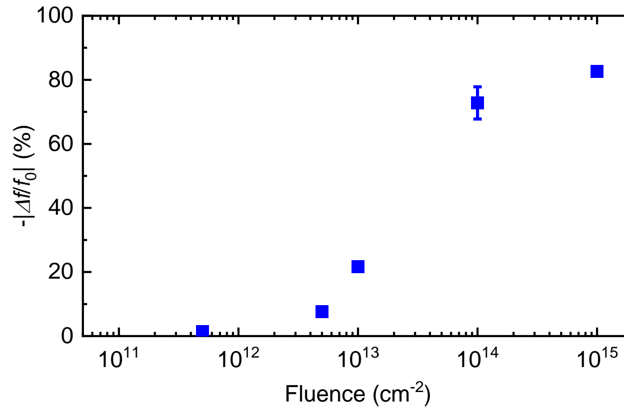

Figure I-10. Fractional downshift of fundamental mode resonance frequency with fluences of 5×10^{11} cm^{-2}, 5×10^{12} cm^{-2}, 10^{13} cm^{-2}, 10^{14} cm^{-2}, and 10^{15} cm^{-2}.

Based on the rectangular cross-sectional shape and orientation of GaN/AlN doubly-clamped structure, the flexural rigidity in the in-plane direction ($E_Y I_z = E_Y t w^3/12$) is more than fifty time larger than that in the out-of-plane direction ($E_Y I_y = E_Y w t^3/12$). Thus, the in-plane mode resonance frequency depends more on E_Y of the material than on the built-in stress σ, compared to the two out-of-plane flexural modes. To study the radiation effect on the Young's modulus of GaN/AlN heterostructure, we measure and model the first in-plane mode resonance of both unirradiated and radiated GaN/AlN doubly-clamped resonators. We first measure the resonance frequencies of the first in-plane mode of the unirradiated devices. The resonance frequencies are centered at 4.419 MHz, 1.398 MHz, 0.770MHz, 0.520 MHz, 0.392 MHz, and 0.314 MHz, respectively, for L = 100, 200, 300, 400, 500, and 600 μm (Fig. I-11a). The measured resonance frequencies before radiation agree well with the analytical model (Eq. 1) by using $E_{Y,GaN}$ = 360 GPa, $E_{Y,AlN}$ = 344 GPa, ρ_{GaN} = 6150 kg/m^3, ρ_{AlN} = 3260 kg/m^3, and σ = 600 MPa. After radiation with fluence of 5×10^{11} cm-

2, the resonance frequencies exhibit slight downshifts. The fractional downshift of resonance frequencies of the first in-plane mode lies within the range of 0.5% and 1.5% (Fig. I-11b).The measured resonance frequencies of the first in-plane mode after radiation agree well with the analytical model (Eq. 1) by using E_Y = 325 GPa. Here $E_Y = (E_{Y,GaN}t_{GaN}+E_{Y,AlN}t_{AlN})/(t_{GaN}+t_{AlN})$. Note that the effect of built-in stress variation is not considered due to its negligible effect. Thus, we observe a 30 GPa decrease of Young's modulus after radiation with fluence of 5×10^{11} cm^{-2}.

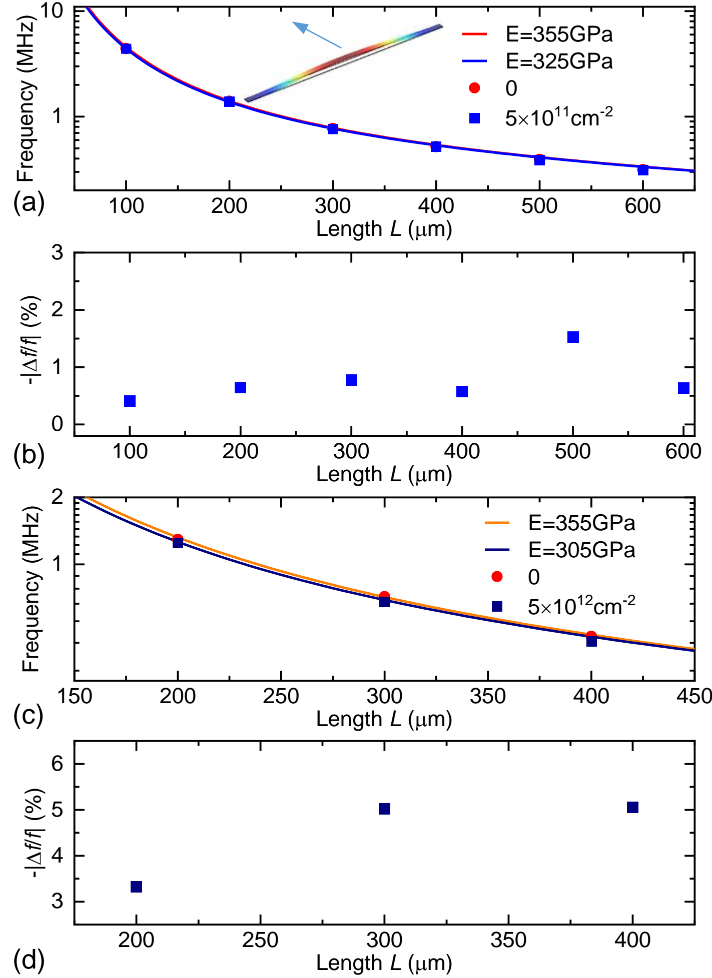

Figure I-11. (a) Resonance frequencies of the first in-plane mode for devices with L = 100, 130, 200, 300, 400, 500, and 600 μm before and after radiation with fluence of 5×10^{11} cm^{-2}. Resonance frequency fitting with elastic resonator model. (b) Fractional downshift of resonance frequency. (c) Resonance frequencies of the first in-plane mode for devices with L = 200, 300, and 400 μm before and after radiation with fluence of 5×10^{12} cm^{-2}. (d) Fractional downshift of resonance frequency.

We then measure the first in-plane mode resonance of the GaN/AlN doubly-clamped resonators with L = 200, 300, and 400 μm before and after radiation with fluence of 5×10^{12} cm^{-2}. Similar to the fundamental mode, Ar+ radiation with fluence of 5×10^{12} cm^{-2} induces much obvious decrease in resonance frequency of the first in-plane mode, with the fractional downshift of resonance frequency lies in the range of 3% and 5% (Fig. I-11c & I-11d). According to the analytical model, Ar^+ radiation with fluence of 5×10^{12} cm^{-2} induces ~50 GPa decrease in the Young's modulus of GaN/AlN heterostructure.

The equation for the multimode resonance frequency of the GaN/AlN doubly-clamped resonator is

$$f_n = \frac{\pi(n+1/2)}{2L^2}\sqrt{\frac{E_Y I}{\rho w t}}\sqrt{1+\frac{0.97\sigma w t L^2}{(n+1)^2\pi^2 E_Y I}}, \qquad (2)$$

where n is the mode number. We measure and model the multimode resonances of unirradiated GaN/AlN doubly-clamped resonators on Chip 3 with different lengths as shown in Fig. I-12. By using $E_{Y,GaN}$ = 360 GPa, $E_{Y,AlN}$ = 344 GPa, ρ_{GaN} = 6150 kg/m^3, ρ_{AlN} = 3260 kg/m^3, and σ = 440 MPa, the analytical model very well agrees with the measured results (Fig. I-12b). For 200 μm long device, a total of five resonant modes are obtained from measurement. By matching the resonance frequencies to finite element method (FEM) simulation results, we confirm that four of them are out-of-plane flexural modes and the other one is in-plane flexural mode, with the corresponding mode shapes shown in Fig. I-12a. The resonance frequencies of out-of-plane modes show a clear "string" behavior, with the frequency ratio to fundamental mode equals to the mode number n.

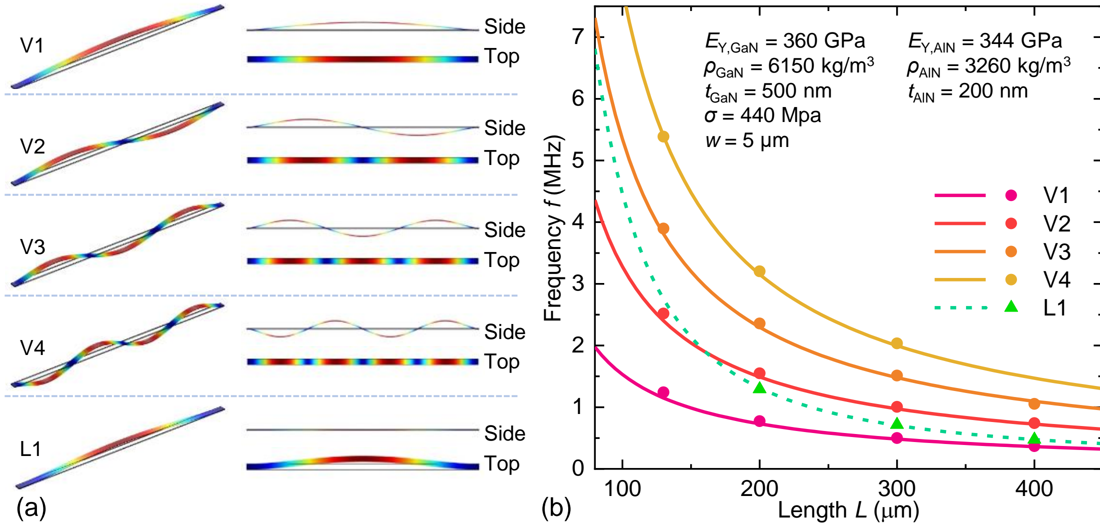

Figure I-12. (a) Mode shapes of four out-of-plane flexural modes (V1, V2, V3, and V4) and one in-plane flexural mode (L1) of GaN/AlN doubly-clamped resonators. (b) Frequency scaling and measured multimode resonance frequencies of unirradiated resonators with different lengths. Symbols represent the measured frequencies while the lines represent the calculated frequencies by theoretical model.

To better understand the effect of radiation on resonant behavior, we further measured the resonance frequency of higher modes of the devices with lengths L= 200, 300 and 400 μm after radiation with high Ar^+ radiation fluences as shown in Fig. I-13. We extract the built-in stress of the devices after radiation via introducing the experimental results into the analytical model. For fluence of 10^{13} cm^{-2}, the built-in stress decrease from 440 MPa to the range of 230 to 400 MPa. Under higher fluence of 10^{14} cm^{-2}, the stress further decreases and lies within the range of 25 to 230 MPa. For the highest fluence of 10^{15} cm^{-2}, we observe significant built-in stress decrease to below 25 MPa. Based on the experimental results and theoretical analysis, we can conclude that the frequency downshifts of the higher modes increases with increase of radiation fluence.

Further, we inspect the GaN/AlN doubly-clamped resonators with high-resolution SEM imaging. While the unirradiated devices appear to be flat in SEM (Fig. I-14a & I-14c), the irradiated GaN/AlN doubly-clamped resonators are severely curved (Fig. I-14b & I-14d), where the amount of curvature varies monotonically with the fluence (Fig. I-14e & I-14f). The results suggest that the irradiation causes mechanical deformation in the GaN/AlN heterostructures resonators.

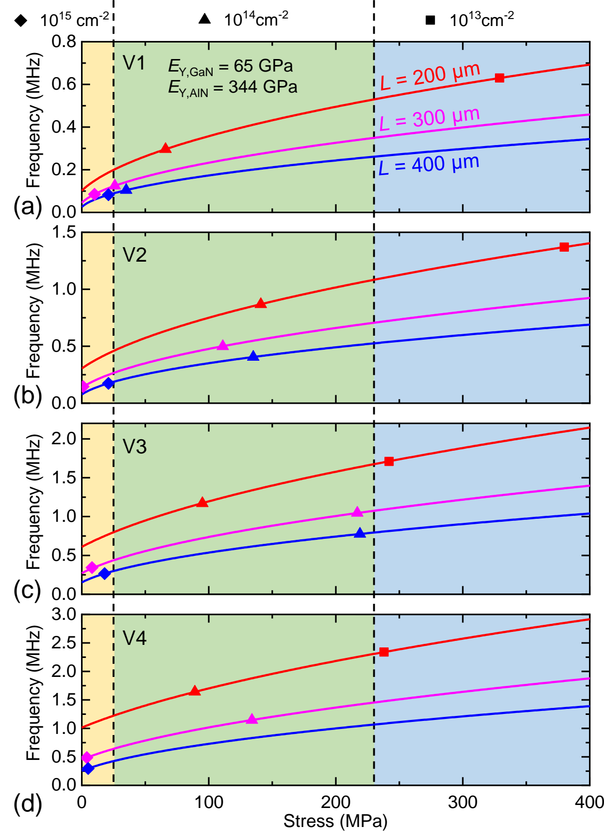

Figure I-13. Effects of high fluence ion irradiation on resonance frequencies of the GaN/AlN MEMS resonators with L = 200, 300, and 400 µm for (a) 1st out-of-plane mode, (b) 2nd out-of-plane mode, (c) 3rd out-of-plane mode and (4) 4th out-of-plane mode. Comparison of measured and calculated fundamental mode resonance frequencies at varying stress with $E_{Y,GaN}$ = 65 GPa.

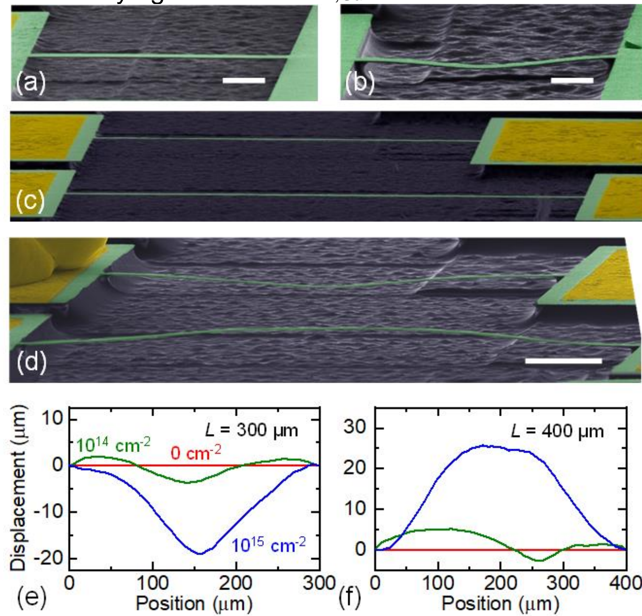

Figure I-14. Post-radiation deformation of GaN/AlN doubly-clamped resonators. Colored SEM image of 130-µm-long resonator (a) without and (b) with 10^{15} cm^{-2} Ar+ irradiation. Scale bars: 20 µm. Colored SEM image of 300 and 400 µm long resonators (c) without and (d) with 10^{15} cm^{-2} Ar+ irradiation. Scale bar: 50 µm. (e)-(f) Profiles of the devices after different fluences of irradiation.

The origin of displacement damage can be ascribed to cumulative non-ionizing radiation damage in the GaN layer. The incident energetic Ar^+ ions collide the lattice atoms and displace them from original lattice positions, resulting in vacancies and interstitials. Due to the channeling effect of GaN, the Ar^+ ions with high energy are slowed down mainly by electronic stopping, while the nuclear stopping become increasingly probable and will dominate the slowing process when ion has sufficiently low velocity. Atoms will be removed from lattice position when they receive enough recoil energy from colliding of ions and a cascade of further collisions occur in the material. Under high fluence of irradiation, extended crystal defects, dislocations and even amorphous layers will be generated. According to SRIM simulation, the displacement damage is confined in the GaN layer, while the AlN layer is intact. Initial stress equilibrium is destroyed in the process and a new stress equilibrium state forms after the radiation. The displacement damage significantly alters Young's modulus and the built-in stress of the GaN/AlN resonators and even causes deformation of the structures at high fluence, which alters the resonance frequency of GaN resonators.

In summary, we have demonstrated the effects of ion-induced displacement damage on doubly-clamped GaN/AlN MEMS resonators with the length L=100, 200, 300, 400, 500, 600, and 700 μm. We irradiate GaN/AlN MEMS devices under 440 keV Ar^+ ions with fluences of 5×10^{11}, 5×10^{12}, 10^{13}, 10^{14}, and 10^{15} cm^{-2}. SRIM simulation shows that all the 440 keV Ar^+ ions stop in the GaN layer and the displacement damage is confined in the 500 nm GaN thin film. The multimode resonances of the devices decrease significantly with the increase of fluence. The fractional downshift of resonance frequencies of fundamental mode lies within the range of 1% and 2.5% at the fluence of 5×10^{11} cm^{-2}. The fractional downshift increases with the fluence, specifically, ~8% downshift for fluence of 5×10^{12} cm^{-2}, ~20% downshift for fluence of 10^{13} cm^{-2}, ~70% downshift for fluence of 10^{14} cm^{-2}, ~80% downshift for fluence of 10^{15} cm^{-2}. SEM shows the irradiated GaN/AlN resonators are severely curved, where the amount of curvature varies monotonically with the fluence. The results suggest that the displacement damage significantly alters Young's modulus and the built-in stress of the GaN/AlN resonators and causes deformation of the structures. The results provide useful information for understanding radiation-induced damage mechanisms in GaN MEMS devices.

(2) Radiation Effects in **β-Ga_2O_3 Nanoelectromechanical Resonators**

a. **Ultraviolet Radiation on β-Ga_2O_3 NEMS Transducers**

We demonstrate a single-crystal β-Ga_2O_3 transducer for solar-blind ultraviolet (SBUV) detection with dual sensing modalities. The device can respond to SBUV based on (i) photocurrent modulation caused by photoelectric effect (Modality I: optoelectronic modality), and (ii) resonance frequency shift induced by photothermal effect (Modality II: NEMS modality). The transducer is fashioned into a suspended channel transistor with metal contacts at source/drain (Fig. I-15a). We examine both the optoelectronic and NEMS modality. The NEMS modality is characterized by both open-loop and closed-loop (oscillator) frequency response to UV irradiation. Finally, we analyze the signal transduction for improving the sensing responsivity.

We fabricate the β-Ga_2O_3 transducer for dual-modality SBUV sensing by using mechanically exfoliated flakes from bulk β-Ga_2O_3 crystal synthesized by edge-defined film-fed growth (EFG) method. After identifying a desired β-Ga_2O_3 flake, we transfer it onto a substrate with pre-defined microtrenches using a dry transfer technique. Subsequently, we deposit metal electrodes (40 nm Au on 150 nm Ti) through a high-precision stencil mask to enhance electrical access to the β-Ga_2O_3 device. The final device has a 5 μm-wide, 32 μm-long, and 310 nm-thick β-Ga_2O_3 channel with a 20 μm-long portion of the channel suspended over the microtrench (Fig. I-15b).

After identifying a candidate nanoflake, we align it to the predefined microtrench under an optical microscope. By pressing down and pulling up the PDMS stamp, the nanoflake is transferred onto the substrate, forming a suspended structure. After the transfer, the device is treated with O_2 plasma for 60 seconds for surface cleaning and activation, followed by deposition of 250 nm Ti, 100 nm Al, and 25 nm Au through a stencil mask. The additional top electrodes enhance mechanical clamping and ensure the electrical contacts at source and drain.

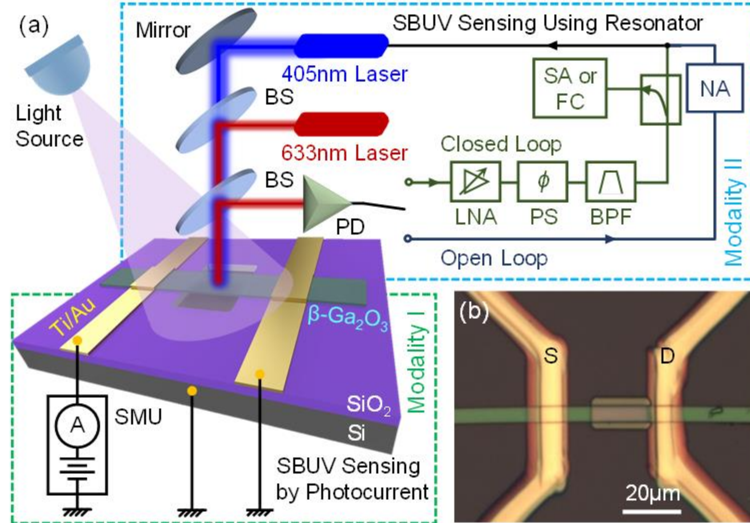

Figure I-15. (a) Schematic illustration of the β-Ga_2O_3 transducer in the form of suspended doubly-clamped beam with electrical contacts for two modalities of SBUV detection, Modality I and Modality II. (b) Optical image of the device.

For Modality I, the electrical conductivity of the β-Ga_2O_3 transducer could be enhanced by modulation of channel conductance and lowering of Schottky barrier height at the β-Ga_2O_3-metal contacts (Fig. I-16a). We measure the photocurrent response of the β-Ga_2O_3 PD using a source measure unit (SMU, Fig. I-15a). Figure I-16b shows the channel current under variable bias upon different LED illumination conditions. The device is only sensitive to SBUV (255 nm) LED illumination. Upon 12 nW of SBUV light irradiation, the device exhibits a current increase of 47.2 pA at V_D = 10V, corresponding to a responsivity of ~4 mA/W. In addition to LEDs, we characterize the response of the PD using a mercury lamp (200–600 nm) and a white light lamp (Fig. I-16c). While the device shows no response to white light, the current increases upon mercury lamp illumination.

In Modality II, the SBUV radiation photothermally heats up the suspended nanostructure. The elevated temperature will expand the device, lower the built-in stress, and downshift the resonance frequency (Fig. I-16d). Therefore, by monitoring the resonance frequency, the incident SBUV irradiation can be resolved. We measure the resonance frequencies of the β-Ga_2O_3 resonator using an ultrasensitive laser interferometry system (Fig. I-15a, Modality II). For the 3rd resonance mode, β-Ga_2O_3 resonator has a resonance frequency of 14.32 MHz and a quality (Q) factor of 1170. The resonance frequency shifts down upon lamp illumination (Fig. I-16e).

We then build a self-sustained oscillator based on the β-Ga_2O_3 resonator (dark green path in Fig. I-15a, Modality II). Further, by illuminating light from the mercury lamp to the β-Ga_2O_3 device periodically, the real-time monitoring of the oscillator shows frequency downshifts upon illumination (Fig. I-16f). Thus we can extract an average responsivity of $\Re_f = \Delta f/P_i \approx 250$ Hz/nW.

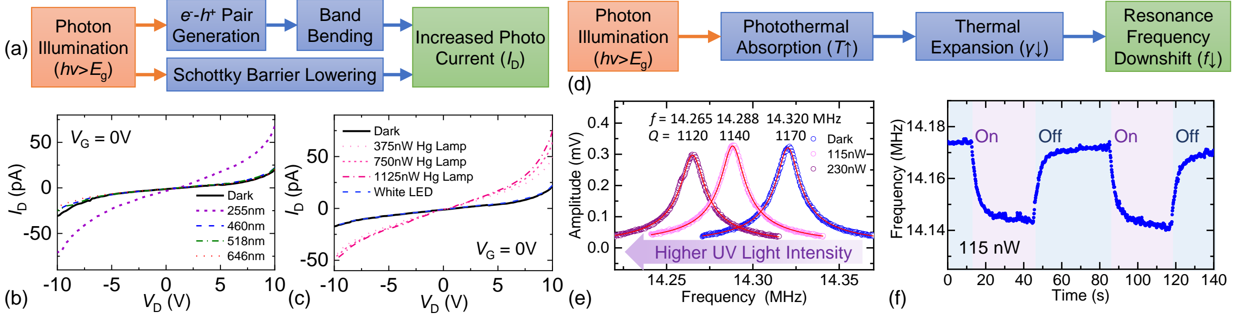

Figure I-16. (a) Signal transduction of SBUV detection using Modality I. (b) Transport characteristics of the PD in dark and upon illumination from (b) different LEDs, and (c) a mercury lamp and a white light lamp. (d) Signal transduction of SBUV detection using Modality II. (e) The frequency response of the 3rd resonance mode upon illumination. (f) Frequency response of the oscillator upon cyclic irradiation.

b. Resonator Platform Characterization for Radiation Measurement

We report on the non-destructive measurement of Young's modulus of single crystal beta gallium oxide (β-Ga_2O_3) out of its nanoscale mechanical structures by measuring their fundamental mode resonance frequencies. Figure I-17a shows a typical β-Ga_2O_3 disk suspended over a circular microtrench with a diameter of d = 5.24 μm. EBSD measurement suggests that the β-Ga_2O_3 flake has its x axis pointing into the substrate (Fig. I-17b), while the y and z directions are along the edges of the β-Ga_2O_3 flake. Using atomic force microscopy (AFM), we determine the thickness of the device as h = 61 nm (Fig. I-17c). By measuring the thermomechanical noise resonance frequency, we resolve a fundamental mode resonance at a frequency of f_0 = 39.6 MHz with a quality (Q) factor of Q = 626 (Fig. I-17d). When the resonance frequency of such disk device is dominated by the flexural rigidity of the suspended structure. The averaged Young's modulus in device plane can be revealed from measured fundamental-mode resonance frequency f_0 by $E_Y = \frac{3\pi^2\rho\left(1-\nu^2\right)d^4}{\left(k_{A0}r\right)^4 h^2} f_0^{\,2}$,where ρ = 5950 kg/m³ is the mass density of β-Ga_2O_3, ν = 0.2 is Poisson's ratio, and $k_{A0}r$ = 3.196 is the eigenvalue for the fundamental mode of a disk resonator clamped at the circular perimeter. We extract a Young's modulus of $E_Y \approx$ 292 GPa for this device.

To further validate the extracted Young's modulus, we measure more β-Ga_2O_3 disk resonators. We measure altogether five β-Ga_2O_3 disk resonators with thickness in 39 to 73 nm range, diameters among 3.20–5.24 μm, and fundamental mode resonance frequencies ranging from 39.6 to 74.9 MHz. Thus, we extract an averaged Young's modulus of $E_{Y,(100)}$ = 261.4±20.6 GPa in (100) plane of β-Ga_2O_3 flakes grown by LPCVD method. Since fundamental mode resonance frequency of β-Ga_2O_3 disk scales linearly with the geometry ratio h/d^2 of the disk (*inset* of Fig. I-17e), we can plot the frequency scaling with respect to h/d^2 using E_Y = 261.4 GPa (Fig. I-17e). All the measured data points are close to the curve, indicating great precision in extraction of Young's modulus using the resonance frequencies of the β-Ga_2O_3 nanodisk resonators.

We use the β-Ga_2O_3 nanobelts that are mechanically cleaved from bulk β-Ga_2O_3 crystal grown by EFG method for fabrication of second series of β-Ga_2O_3 devices. Based on the bonding strength of different planes of monoclinic β-Ga_2O_3 crystal, the largest surface of the β-Ga_2O_3 nanobelt is in parallel with the (100) plane of β-Ga_2O_3 crystal and the [010] direction (y axis) goes along with the longest sides of the nanobelt. Figure I-17f shows a typical β-Ga_2O_3 doubly-clamped beam resonator. The device is 460 nm thick, suspended over a 20.6 μm long microtrench. Figure I-17g shows the photothermally driven resonance spectrum of the fundamental mode resonance. Similar to the β-Ga_2O_3 disk resonators, Young's modulus of the doubly-clamped beam can be

extracted from measured first mode resonance frequency when the resonance motion of the device is dominated by the flexural rigidity of the structure. Therefore, we have $E_{\mathrm{Y}} = \frac{48\pi^2 \rho L^4}{(k_{\mathrm{B0}}L)^4 h^2} f_0^{\,2}$, where L is the length of the doubly-clamped beam and $k_{\mathrm{B0}}L = 4.73$ is the eigenvalue for the fundamental mode of a doubly-clamped beam. In this case, we can extract Young's modulus along the [010] direction (y axis) of β-Ga_2O_3 crystal. We have an averaged Young's modulus of $E_{\mathrm{Y}} = 245.8\pm9.2$ GPa along [010] direction (y axis) out of 3 devices. The fundamental mode resonance frequencies of β-Ga_2O_3 doubly-clamped beams scale linearly with the geometry ratio h/L^2 (*inset* of Fig. I-17h). Thus we can also confirm the precision of Young's modulus extraction for doubly-clamped beams with the results in Fig. I-17h.

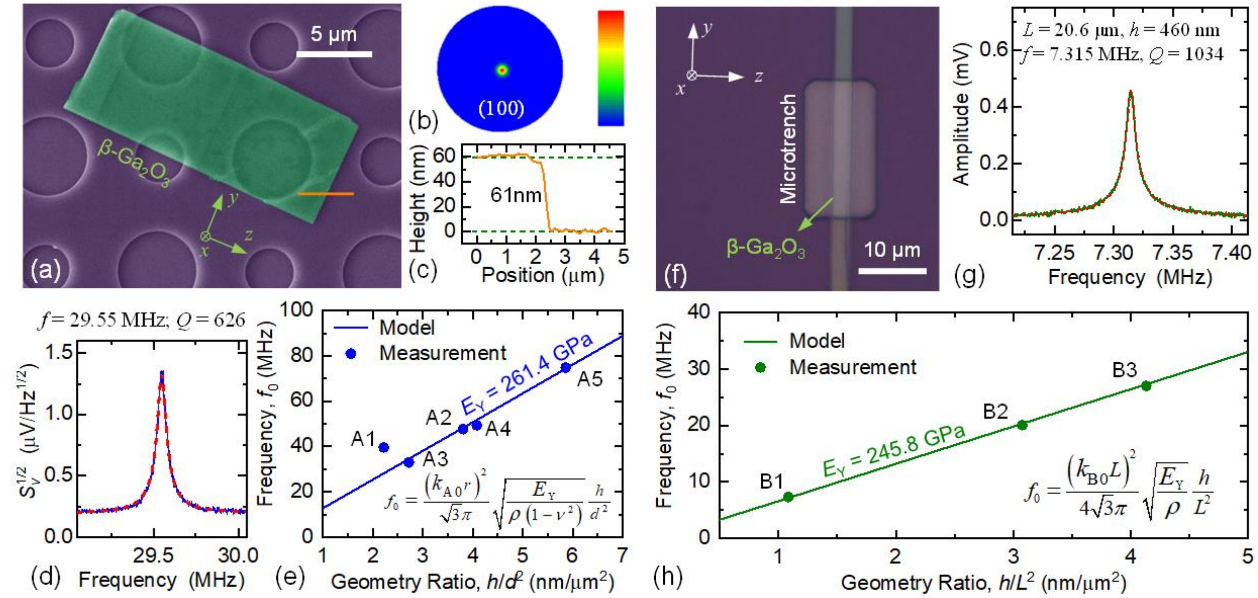

Figure I-17. (a-e) Young's modulus extraction from β-Ga_2O_3 disk resonators. (a) A colored SEM image of a β-Ga_2O_3 disk resonator. Coordinate labels indicate x, y, and z directions acquired from EBSD measurement. (b) EBSD pole figure for (100) plane of the device. (c) AFM trace corresponding to the orange line in (a). (d) Fundamental mode resonance spectrum. (e) Frequency scaling with respect to geometry ratio h/d^2 using the extracted Young's modulus ($E_{\mathrm{Y}} = 261.4$ GPa). (f-h) Young's modulus extraction from β-Ga_2O_3 doubly-clamped beam resonators. (f) Optical image of a β-Ga_2O_3 doubly-clamped beam resonator. Coordinate labels indicate x, y, and z directions based on the orientation of the β-Ga_2O_3 nanobelt. (g) Fundamental mode resonance spectrum of the doubly-clamped resonator. (h) Frequency scaling with respect to geometry ratio h/L^2 using the extracted Young's modulus ($E_{\mathrm{Y}} = 245.8$ GPa).

Equivalent circuit modeling of electromechanical devices plays crucial roles in evaluating the device operation in complex circuits, in simulating their performance when interfacing with electronic devices, and toward electronic design automation (EDA) for large scale integration and manufacturing. We develop the small signal equivalent circuit model of a β-Ga_2O_3 vibrating channel transistor (VCT) and simulate the circuit in Cadence design tool. Figure I-18 shows the equivalent circuit and comparison of output current i between Cadence simulation and analytical calculation. The current from capacitive branch of the circuit i_{cap} contributes to the majority of i (Fig. I-18c and I-18d). The field-effect current i_{FE} can gain dominance by significantly boosting g_{m} (= 1 μS) of the transistor (Fig. I-18e), which could be achieved by using suspended modulation-doped field effect transistor (MODFET) structure.

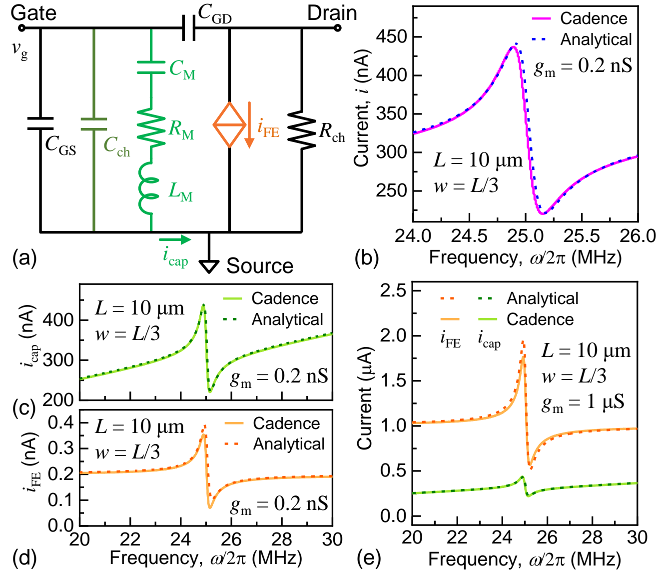

Figure I-18. Analytical model and Cadence simulation of a β-Ga_2O_3 VCT. (a) Small signal equivalent circuit model used for Cadence simulation, with gate-channel capacitance C_{ch}, parasitic capacitances C_{GD} and C_{GS}, motional components $C_m = \eta^2/k_{eff}$, $R_m = \sqrt{k_{eff}M_{eff}}/(Q\eta^2)$, and $L_m = M_{eff}/\eta^2$, where k_{eff} is the effective spring constant and $\eta = C_{ch}V_G/z_0$, current in capacitive branch i_{cap}, and field effect current $i_{FE} = g_m(v_{RF} - \delta z V_G/z_0)$. (b) Comparison of i by analytical model and Cadence simulation. (c) Magnitude of i_{cap} and (d) i_{FE} from analytical model and Cadence simulation, respectively. (e) i_{FE} dominates in the VCT with boosted g_m = 1 μS.

The experimental characterization of Young's modulus β-Ga_2O_3 set the baseline to study the displacement damage effect on mechanical properties of β-Ga_2O_3 M/NEMS devices and the construction of equivalent circuit model of β-Ga_2O_3 VCT could help develop the *in situ* measurement of β-Ga_2O_3 resonant M/NEMS devices under radiation. These efforts serve as essential building blocks for upcoming experimental investigation in radiation effect on β-Ga_2O_3 M/NEMS devices.

(3) ***In-Situ* Electrical Measurement of Proton Radiation Effects on Si MEMS Resonators**

We report on in-situ measurement of proton radiation effects on single-crystal silicon comb-drive resonant microelectromechanical systems (MEMS). The comb-drive resonators are specially designed and can be operated in both linear and contact-impacting (*i.e.*, 'tapping') modes, which offer versatile options for resonant sensing and switching applications. *In-situ*, continuous monitoring of radiation effects induced by impinging 1.8MeV protons with controlled dosage and exposure time, in both linear and tapping modes of the resonators, have been performed. The resonators exhibit highly sensitive responses in resonance characteristics while maintaining robust operations. For irradiation with a proton flux of 2.8×10^8cm^{-2}s^{-1}, both temporary and permanent radiation effects (*i.e.*, frequency shift) on the comb-drive MEMS resonators are observed. For irradiation with much higher flux (9.1×10^8cm^{-2}s^{-1}), the resonance frequency shifts are greater. Based on the transport of ions in matter (TRIM) simulations, we find that the observed radiation effects on resonance frequency could be attributed to a combination of ionizing and displacement damage effects. These in-situ observations of radiation effects on comb-drive MEMS resonators show that dynamical MEMS capable of operating in different resonance regimes can be a promising platform for making new types of radiation sensors or radiation-hardened signal processing components.

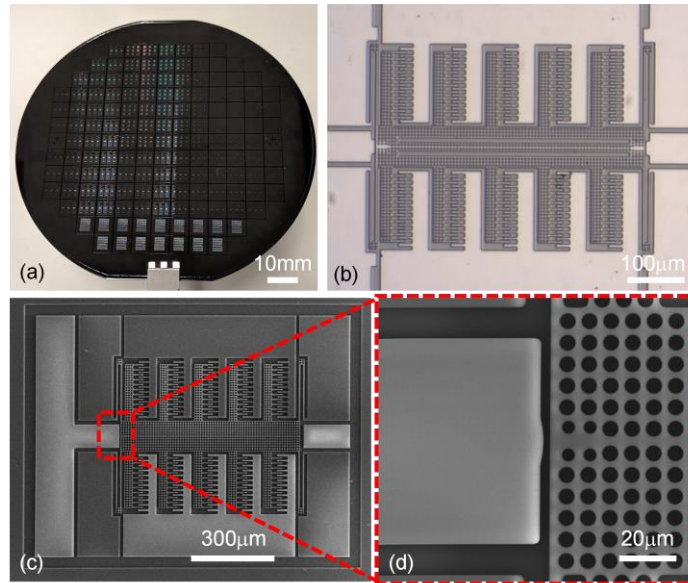

Figure I-19. Fabricated SOI comb-drive MEMS resonators. (a) 4-inch wafer after Si etching. (a) Optical and (c) SEM image of typical SOI comb-drive MEMS resonators. (d) SEM image of the stopper for tapping mode operation. The location of the stopper in the resonator is marked in (c). An initial gap between the stopper and the shuttle is 2μm.

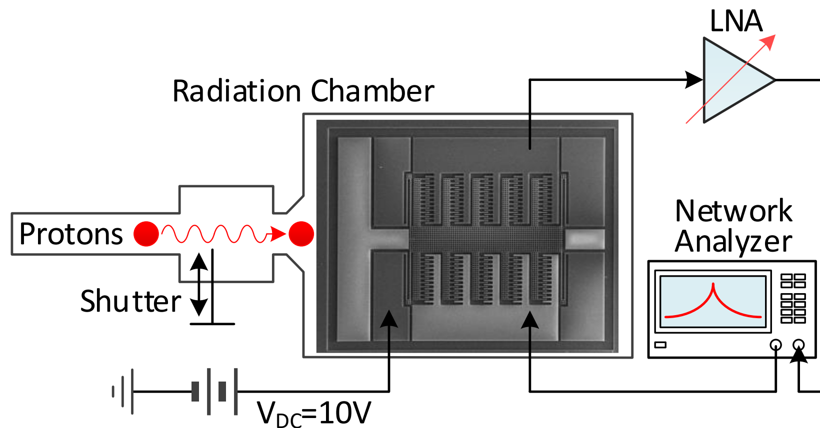

Figure I-20. Schematic of the in-situ measurement system of 1.8MeV proton radiation effects on comb-drive MEMS resonators. Resonance responses of the devices are obtained by using a two-port transmission measurement. Radiation exposure time is controlled by opening and closing a shutter.

After the device fabrication, the MEMS resonators are located inside the vacuum chamber of the Vanderbilt University Pelletron to monitor proton radiation effects *in-situ* (Fig. I-20). The fabricated chip is mounted in the vacuum chamber, and the devices are electrically connected via feedthrough to resonance measurement apparatus located in the outside of the vacuum chamber. The position and angle of the chip in the vacuum chamber are carefully adjusted using a positioning stage so that the devices are located in the center of the proton beam, and they are irradiated with normal-incidence protons. The performance of the device is calibrated by using a two-port transmission measurement. A polarization DC voltage (V_{DC} = 10V) is applied to the comb-drive shuttle, an AC voltage from a network analyzer is introduced to the comb-drive fingers. The electrostatic force induced by both the DC and AC signals excites resonance motion, and the transmission of the AC signal is measured through the comb-drive fingers using the network analyzer. The output signal from the device is amplified by employing a low-noise preamplifier

with a voltage gain of 20. During the resonance measurement, we adjust frequency sweep time of the network analyzer to be much slower than ringdown response of the resonance to avoid any measurement artifact associated with a high Q factor of the device.

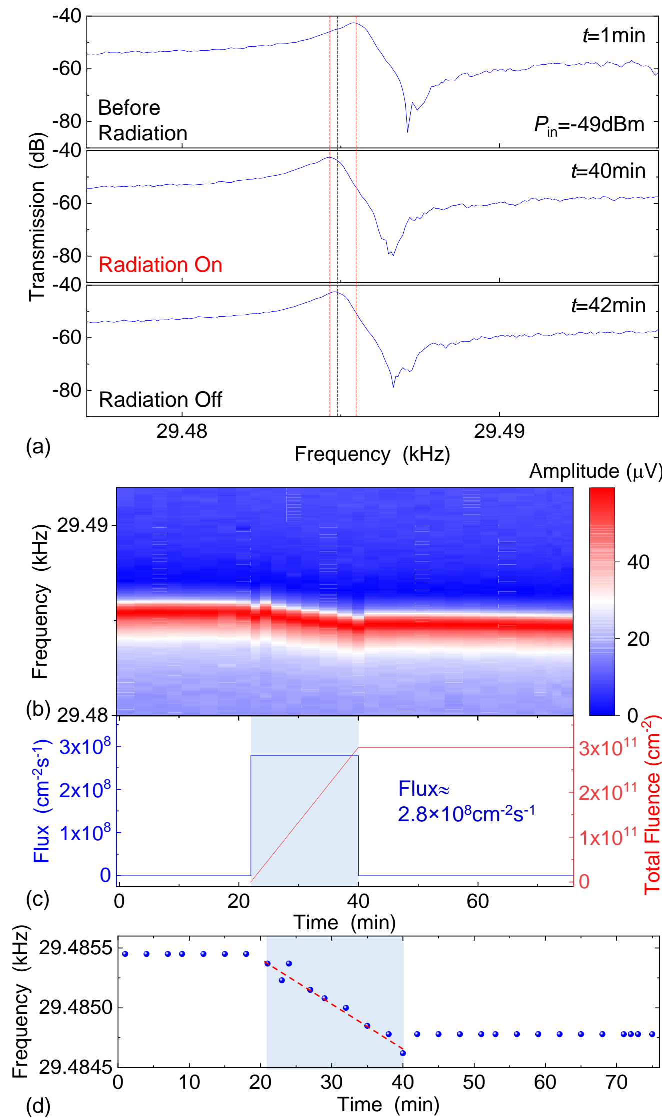

Figure I-21. 1.8MeV proton radiation effects on a SOI comb-drive MEMS resonator operating in linear mode. Proton flux is set to be 2.8×10^{8}cm^{-2}s^{-1}. (a) Measured individual resonance before, during, and after radiation. Red vertical dashed lines represent the resonance frequency of the three curves, indicating frequency shifts. (b) Color map of the measured resonance over experiment time. (c) Proton radiation profile, including proton flux and fluence over time. (d) Resonance frequency during the measurement. Blue areas in (c) and (d) represent the period when the shutter is open, and thus the SOI come-drive MEMS resonator is exposed to the 1.8MeV proton radiation. Red dashed line in (d) shows a linear fit.

After the pre-irradiation resonance measurement, we then focus on performing *in-situ* measurement of 1.8MeV proton radiation effects on the SOI comb-drive MEMS resonator. Among the multiple comb-drive MEMS resonators fabricated on the chip, the device located in the center of the chip is electrically connected to the resonance measurement apparatus shown in Fig. I-20 to monitor *in-situ* radiation effects. The driving strength is controlled between P_{in} = –49dBm and –45dBm to monitor radiation effects on both the linear and tapping mode operations. The proton

radiation energy and flux from the source are set to be 1.8MeV and 2.8×10^{8}cm^{-2}s^{-1}, respectively, and they are precisely calibrated using a conventional radiation detector in the chamber.

Figure I-21a shows the measured resonance before, during, and after the proton irradiation, showing clear resonance frequency shifts in the linear regime. First, we track the resonance frequency over ~22 min without exposing the device to radiation to check the stability of the device, and the device shows excellent frequency stability ($\delta f \approx 0.03$Hz) over the measurement time (Fig. I-21b and I-21d). Next, we open the shutter between the radiation source and the chamber (Fig. I-20) and expose the device to 1.8MeV proton irradiation in vacuum at room temperature. During the exposure to radiation, the resonance frequency linearly shifts down, and we find a frequency shift of $\Delta f = -0.7$Hz after 1080s exposure (Fig. I-21b). The total fluence is ~3.0×10^{11}cm^{-2}. Then we quickly close the shutter to stop the proton impingement on the device. Immediately after stopping proton irradiation, the resonance frequency quickly upshifts by ~0.1Hz, resulting in the permanent resonance frequency shift of $\Delta f = -0.6$Hz compared to the frequency before exposure to radiation. Once resonance returns, the resonance is stable, and it does not show further noticeable frequency shift. These very small frequency shifts are discernable thanks to the excellent frequency stability of the devices. We have also studied radiation effects on the Q factor of the device. As shown in Fig. I-21a and I-21b, 3dB linewidth of the resonance curve is quite consistent, showing the Q factor is not influenced by the proton radiation.

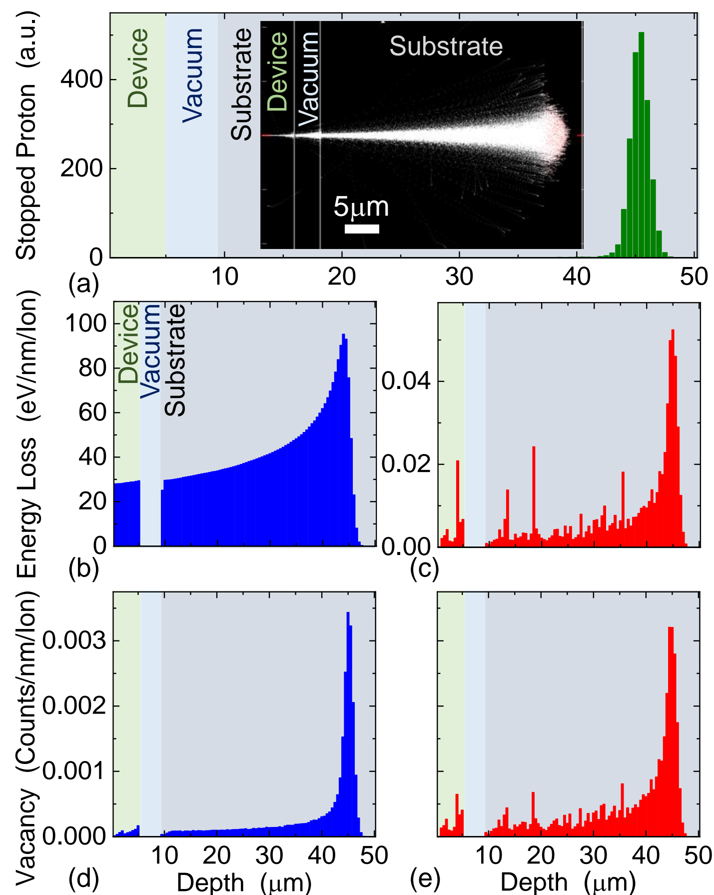

Figure I-22. SRIM simulated interactions between 1.8MeV proton radiation and the MEMS device structure. (a) Proton distribution stopped in the device structure. Inset shows proton trajectory. Computed energy loss profile from (b) ions and (c) recoils. Vacancy distribution induced by displacement damage from (d) ions and (e) recoils.

To further understand the measured proton radiation effects on the comb-drive MEMS devices, we have performed the transport of ions in matter (TRIM) simulations using a stopping and range of ions in matter (SRIM) code. With energy of 1.8MeV the protons have a stopping depth of ~46μm from the top surface of the device (Fig. I-22a). The proton irradiation can ionize atoms in the device structure, generating charges. Figure I-22b and I-22c show the simulated energy loss profile due to ionizing effects. We find that 8.0% and 92% of energy loss occurs in the device layer and Si substrate, respectively. The different amounts of ionization effects between the device and substrate create additional potential and thus added polarization voltage during radiation. This potential then introduces electrostatic forces and capacitive softening effects, showing the frequency jumps down when we open the shutter and start proton irradiation. After the exposure to radiation, the generated charges and trapped ions quickly neutralize since the substrate is connected to ground, and thus the resonance frequency jumps back. Besides, from the TRIM simulation, we find vacancy generation during the irradiation. Figure I-22d and I-22e show a simulated depth profile of the vacancy density created by the displacement damage from ions and recoils. The displacement damage and vacancies creation modify the Si crystal lattice and thus degrade mechanical properties such as reduction of E_Y. We find that most vacancies are created at the proton stopping depth of ~46μm and 4.5% of vacancies are created in the device layer. During the exposure to radiation, proton impingements continuously damage the Si crystal and thus decrease E_Y, leading to the gradual downshift of the resonance frequency. Based on analytical modeling, we find that E_Y of the device is reduced by 0.022% after exposure to radiation. Once crystal lattice is damaged, it cannot be easily recovered at room temperature, giving permanent frequency shifts.

We further simulate the radiation effects on thicker MEMS devices. From the TRIM simulation for a 10μm-thick MEMS resonator, we find that 16.2% of energy loss occurs and 8.0% of the vacancies are created in the device layer, almost twice higher than the results in the 5μm-thick device. Our simulation results indicate that thicker MEMS devices will have more pronounced radiation effects, both ionizing effects and displacement damage, which could be useful to make ultrasensitive resonant radiation sensors.

In summary, we have performed *in-situ* experiments of radiation effects on MEMS resonators by impinging 1.8MeV protons on single-crystal SOI comb-drive resonators. The devices are operated in both linear regime and tapping mode, and we find temporary and permanent frequency shifts during and after proton radiation. From TRIM simulation, we show that both displacement damage and ionizing effects play significant roles in frequency shifts. The study shows that MEMS resonators offer excellent radiation sensing capability, while sustaining their functions in various regimes. Taking advantage of radiation sensitivity and tolerance, we envision MEMS resonators, when operated in different regimes, can be employed under certain conditions in proton radiation environment as either ultrasensitive radiation detectors or radiation-hardened signal processing components.

What opportunities for training and professional development has the project provided?
If the research is not intended to provide training and professional development opportunities or there is nothing significant to report during this reporting period, state "Nothing to Report." Describe opportunities for training and professional development provided to anyone who worked on the project or anyone who was involved in the activities supported by the project. "Training" activities are those in which individuals with advanced professional skills and experience assist others in attaining greater proficiency. Training activities may include, for example, courses or one-on-one work with a mentor. "Professional development" activities result in increased knowledge or skill in one's area of expertise and may include workshops, conferences, seminars, study groups, and individual study. Include participation in conferences, workshops, and seminars not listed under major activities.

The following are main training and professional development activities enabled by this project:

Prof. Philip Feng (UF, PI) has given a number of invited talks, invited tutorials, and invited seminars on SiC MEMS/NEMS and new NEMS and other nanodevices enabled by 2D semiconducting crystals in the past year. He has mentored a few Ph.D. graduate students, 1 undergraduate student involved in this program (through the basic program period and the option year period), and also supervised 2 postdoc research associates/scientists who participated in this project.

Wen Sui (UF) is a 4th year Ph.D. student in Prof. Philip Feng's group in ECE at UF. He has received solid training during past 3 years on SiC, GaN, and Ga_2O_3 MEMS/NEMS design, modeling/simulation, fabrication, and characterization. He is also studying materials physics of SiC crystals and radiation sources and radiation physics. He is working on testing SiC, GaN and Ga_2O_3 MEMS/NEMS and their radiation effects. As the 1st author, he has contributed 3 journal articles in important and high-impact journals (*JMEMS 2021*, *IEEE TNS 2022*, *Advanced Functional Materials 2022*), 4 conference papers (*IEEE MEMS 2021*, *NSREC 2021*, *IFCS 2021, HiTEN 2022*). He has been selected as one of the four ***Finalists for the Best Student Paper Award Competition*** at the *IEEE IFCS 2021* in July 2021. For his excellent research progress and achievements, Wen Sui has been awarded the *2022 UF IMG Excellence in Research Award* (IMG: Interdisciplinary Microsystems Group at UF, https://www.img.ufl.edu/).

Dr. Jaesung Lee (UF) has been an assistant research scientist in ECE at UF during the performance of this project. He has received solid training of performing *in-situ* radiation experiments in Vanderbilt Pelletron system. He has working on characterization of SiC MEMS/NEMS and Si SOI comb-drive resonators/oscillators and their proton radiation effects. He has authored 2 conference papers and 1 journal article based on the outcomes of this program.

Dr. Xu-Qian Zheng (UF) has been a postdoctoral research associate in Prof. Philip Feng's group. Through the project, he has gained further knowledge on radiation effects on semiconductors and MEMS and NEMS devices. He has delivered several conference presentations and 2 journal articles about radiation effects on β-Ga_2O_3 and GaN MEMS and NEMS devices, respectively.

Prof. Michael Alles (Vanderbilt, Co-PI) has given several invited talks and tutorials on Radiation Effects in Advanced Nanoelectronics and in MEMS/NEMS in the last year. He mentors several Ph.D. and M.S. graduate students involved in this project. The Vanderbilt University graduate students participated in training for use of Vanderbilt radiation sources, fabrication and characterization tools, and simulation tools.

How have the results been disseminated to communities of interest?
If there is nothing significant to report during this reporting period, state "Nothing to Report." Describe how the results have been disseminated to communities of interest. Include any outreach activities that have been undertaken to reach members of communities who are not usually aware of these research activities, for the purpose of enhancing public understanding and increasing interest in learning and careers in science, technology, and the humanities.

This project has generated many high-quality journal articles and refereed conference papers. (Underlined Names are PI **Philip Feng**'s Advisees at UF or CWRU; PI's Name in **Bold** Font)

a. Journal Articles (all peer-reviewed)

[J10] H. Jia, J. P. McCandless, H. Chen, W. Liao, E. X. Zhang, M. W McCurdy, R. A. Reed, R. D. Schrimpf, M. A. Alles, and **P. X.-L. Feng**, "Proton Radiation Effects on Optically Transduced Silicon Carbide Microdisk Resonators", *Optical Materials Express* (2022). Under Review.

[J9] J. Lee, M. W. McCurdy, R. A. Reed, R. D. Schrimpf, M. A. Alles, and **P. X.-L. Feng**, "*In-Situ* Measurement of 1.8MeV Proton Radiation Effects on Comb-Drive MEMS Resonators", *IEEE Transactions on Nuclear Science* (2022). In Revision.

[J8] W. Sui, H. Wang, J. Lee, A. Qamar, M. Rais-Zadeh, and **P. X.-L. Feng**, "AlScN-on-SiC Thin Film Micromachined Resonant Transducers Operating in High-Temperature Environment up to 600°C", *Advanced Functional Materials* **32**, 2202204 (2022). DOI: https://doi.org/10.1002/adfm.202202204.

[J7] [*Invited Perspective Article*] X.-Q. Zheng, H. Zhao, and **P. X.-L. Feng**, "A Perspective on β-Ga_2O_3 Micro/Nanoelectromechanical Systems", *Applied Physics Letters* **120**, 040502 (2022). DOI: 10.1063/5.0073005. [*Featured as **Editor's Pick***]

[J6] W. Sui, X.-Q. Zheng, J.-T. Lin, J. Lee, J. Davidson, R.A. Reed, R.D. Schrimpf, B.W. Alphenaar, M. L. Alles, and **P. X.-L. Feng**, "Effects of Ion-Induced Displacement Damage on GaN/AlN MEMS Resonators", *IEEE Transactions on Nuclear Science* **69**, 521-529 (2022). DOI: 10.1109/TNS.2022.3143550.

[J5] X.-Q. Zheng, H. Zhao, Z. Jia, X. Tao, and **P. X.-L. Feng**, "Young's Modulus and Corresponding Orientation in β-Ga_2O_3 Thin Films Resolved by Nanomechanical Resonators", *Applied Physics Letters* **119**, 013505 (2021). https://doi.org/10.1063/5.0050421

[J4] W. Sui, X.-Q. Zheng, J.-T. Lin, B.W. Alphenaar, and **P. X.-L. Feng**, "Thermal Response and TC*f* of GaN/AlN Heterostructure Multimode Micro String Resonators From -10 °C Up to 325 °C", *Journal of Microelectromechanical Systems* **30**, 521-529 (2021). DOI: 10.1109/JMEMS.2021.3089703

[J3] X.-Q. Zheng, T. Kaisar, and **P. X.-L. Feng**, "Electromechanical Coupling and Motion Transduction in β-Ga_2O_3 Vibrating Channel Transistors", *Applied Physics Letters* **117**, 243504 (2020). DOI: 10.1063/5.0031503.

[J2] R. Yang, J. Qian, and **P. X.-L. Feng**, "Electrodynamic Force, Casimir Effect, and Stiction Mitigation in Silicon Carbide Nanoelectromechanical Switches", *Small* **16** (51), 2005594 (2020). DOI: 10.1002/smll.202005594.

[J1] H.-L. Chen, H. Jia, C.A. Zorman, and **P. X.-L. Feng**, "Determination of Elastic Modulus of Silicon Carbide (SiC) Thin Diaphragms via Mode-Dependent Duffing Nonlinear Resonances", *Journal of Microelectromechanical Systems* **29**, 783-789 (2020). DOI: 10.1109/JMEMS.2020.3020568.

b. Conference Papers and Presentations (all peer-reviewed)

[C12] J. Lee, M. W. McCurdy, R. A. Reed, R. D. Schrimpf, M. L. Alles, and **P. X.-L. Feng**, "*In-Situ* Measurement of 1.8MeV Proton Radiation Effects on Comb-Drive MEMS Resonators", *2022 IEEE Nuclear and Space Radiation Effects Conference (NSREC 2022)*, Provo, UT, Jul. 18-22 (2022).

[C11] W. Sui, H. Wang, J. Lee, A. Qamar, M. Rais-Zadeh, and **P. X.-L. Feng**, "AlScN-on-SiC Diaphragm Multimode Micromechanical Resonators for High-Temperature Sensing Applications", *2022 IMAPS Int. Conference & Exhibition on High Temperature Electronics Network (HiTEN 2022)*, Oxford UK & Online (Hybrid), Jul. 18-20 (2022).

[C10] W. Sui, X.-Q. Zheng, J.-T. Lin, J. Davidson, R.A. Reed, R.D. Schrimpf, B.W. Alphenaar, M. L. Alles, and **P. X.-L. Feng**, "Effects of Ion-Induced Displacement Damage on GaN/AlN MEMS Resonators", *2021 IEEE Nuclear and Space Radiation Effects Conference (NSREC 2021)*, Virtual Conf., Jul. 16-23 (2021).

[C9] R. Yang, M. Xie, Y. Jia, L. Duraffourg, and **P. X.-L. Feng**, "Hybrid Nanoelectromechanical Switch and Resistive Memory in Silicon Nanowires by VLSI NEMS", *Proc. 34th IEEE Int. Conf. on Micro Electro Mechanical Systems (MEMS 2021)*, pp. 607-610, Online, Jan. 25-29 (2021).

[C8] W. Sui, X.-Q. Zheng, J.-T. Lin, B.W. Alphenaar, and **P. X.-L. Feng**, "Temperature Dependence of Multimode Gallium Nitride/Aluminum Nitride (GaN/AlN) Heterostructure String Resonator", *Proc. 34th IEEE Int. Conf. on Micro Electro Mechanical Systems (MEMS 2021)*, pp. 478-481, Online, Jan. 25-29 (2021).

[C7] X.-Q. Zheng and **P. X.-L. Feng**, "Temperature Coefficient of Resonance Frequency (TC*f*) of β-Ga_2O_3 Nanomechanical Resonators", *Proc. 34th IEEE Int. Conf. on Micro Electro Mechanical Systems (MEMS 2021)*, pp. 165-167, Online, Jan. 25-29 (2021).

[C6] X.-Q. Zheng and **P. X.-L. Feng**, "Equivalent Circuit Modeling of Beta Gallium Oxide (β-Ga_2O_3) Vibrating Channel Transistors", *2020 IEEE International Ultrasonics Symposium (IEEE IUS 2020)*, Virtual Conf., Sept. 6-11 (2020).

[C5] J. Lee, Y. Xie, M. W. McCurdy, M. L. Alles, and **P. X.-L. Feng**, "*In-Situ* Proton Radiation Sensing Using Comb-Drive MEMS Resonators", *2020 Joint Conference of IEEE International Frequency Control Symposium and International Symposium on Applications of Ferroelectrics (IEEE IFCS-ISAF 2020)*, Virtual Conf., Jul. 19-23 (2020).

[C4] X.-Q. Zheng, Y. Xie, J. Lee, and **P. X.-L. Feng**, "Dual-Modality Solar Blind Ultraviolet Detection Using a Beta Gallium Oxide (β-Ga_2O_3) Transducer", *2020 Joint Conference of IEEE International Frequency Control Symposium and International Symposium on Applications of Ferroelectrics (IEEE IFCS-ISAF 2020)*, Virtual Conf., Jul. 19-23 (2020).

[C3] X.-Q. Zheng, J. Lee, and **P. X.-L. Feng**, "Toward Enhanced Electrical Readout of β-Ga_2O_3 Nanoelectromechanical Resonators", *2020 Joint Conference of IEEE International Frequency Control Symposium and International Symposium on Applications of Ferroelectrics (IEEE IFCS-ISAF 2020)*, Virtual Conf., Jul. 19-23 (2020).

[C2] [*Invited Paper & Talk*] **P. X.-L. Feng**, "Resonant Nanoelectromechanical Systems (NEMS): Progress and Emerging Frontiers", *Proc. 33rd IEEE Int. Conf. on Micro Electro Mechanical Systems (MEMS 2020)*, pp. 212-217, Vancouver, Canada, Jan. 18-22 (2020).

[C1] X.-Q. Zheng, J. Lee, **P. X.-L. Feng**, "Beta Gallium Oxide (β-Ga_2O_3) Vibrating Channel Transistor", *Proc. 33rd IEEE Int. Conf. on Micro Electro Mechanical Systems (MEMS 2020)*, pp. 186-189, Vancouver, Canada, Jan. 18-22 (2020).

The above lists show main outcomes in the performance period 08/14/2019 – 02/19/2022.

During this period, the cumulative total outcome includes 10 journal papers/manuscripts and 12 conference papers, and 2 student paper award or research excellence recognitions.